
WIDEFIELD QUANTUM MICROSCOPY WITH SOLID-STATE SPIN DEFECTS: NEW INSTRUMENTS, MATERIALS, AND APPLICATIONS

GABRIEL JAN ABRAHAMS

 0000-0002-2360-7150

UNDER THE JOINT SUPERVISION OF

DR. JEAN-PHILIPPE TETIENNE

AND

DR. DAVID SIMPSON

*SCHOOL OF PHYSICS
THE UNIVERSITY OF MELBOURNE*



SUBMITTED AS A PARTIAL REQUIREMENT FOR THE DEGREE OF
MASTER OF SCIENCE (PHYSICS)

12 NOVEMBER 2021

Statement of Contribution and Originality

This statement is to certify that the following work is all original and completed by the Author, unless otherwise specified. Chapter 1 provides an original review of conventional quantum diamond microscopy to provide context to the specialised systems we describe in later chapters. All experimental work detailed in Chapters 2, 3 and 4 are the author's except where stated otherwise.

A substantial portion of the work reported in Chapter 2 appears in the following paper and its supplementary material, which I wrote and edited, with few changes:

G. J. Abrahams, S. C. Scholten, A. J. Healey, I. O. Robertson, N. Dotschuk, S. Q. Lim, B. C. Johnson, D. A. Simpson, L. C. L. Hollenberg, J.-P. Tetienne, *An Integrated Widefield Probe for Practical Diamond Nitrogen-Vacancy Microscopy*, Submitted to Applied Physics Letters (2021), available arXiv:2109.14388.

A portion of the discussion in Chapter 2 includes a section I wrote and edited of the following paper, with few changes:

S. C. Scholten, A. J. Healey, I. O. Robertson, **G. J. Abrahams**, D. A. Broadway, J.-P. Tetienne, *Wide-field quantum microscopy with nitrogen-vacancy centers in diamond: strengths, limitations, and prospects*, Accepted to Journal of Applied Physics (2021), available arXiv:2108.06060.

A portion of the work presented in Chapter 4 appears in the following paper:

S. C. Scholten, **G. J. Abrahams**, B. C. Johnson, A. J. Healey, I. O. Robertson, J. Bullock, J.-P. Tetienne, *Magnetic photocurrent imaging of open-circuit current paths in silicon photovoltaic devices with a widefield nitrogen-vacancy microscope*, Manuscript in preparation.

Acknowledgements

The sheer number of hours J.-P. has invested in teaching, mentoring and coaching me are beyond any expectations a student could have. I can only begin to express my gratitude for this dedication to my education, and admiration that he finds the time and energy to do it so well, amongst so many other research and teaching commitments. If I can convince someone my research is interesting, it is because J.-P. taught me how to tell a story.

Thank you to Sam Scholten for answering all my questions, guiding me through this experience, giving me confidence, and providing thoroughly entertaining feedback. Thank you to Dr. David Simpson for all his guidance. Thank you to Dr. Nikolai Dotschuk for useful discussions, and training.

It's been a pleasure getting to know all my quantum sensing colleagues, it's been great fun to catch up socially whenever we can in person, and virtually otherwise. Thanks to Alex Healey, Alister Chew, Charlie Pattinson, Dan McCloskey, Di Wang, Ella Walsh, Erin Grant, Greg White, Robert de Gille and Scott Lillie. Special thanks to my friend and colleague Islay Robertson.

Thank you to Janet Newman for her brilliant mentorship over many years, and feedback.

I am immensely grateful for the support and camaraderie of all my friends and physics colleagues. In particular Matthew Bunney. Thank you also to Adam Kues, Ben Harper, Chris Nakhl, Joseph Bloom and Elodie Higgins, and the many other friends who I've had the privilege of knowing throughout my undergraduate and graduate degree.

Thank you to Cara Faulkner for her companionship, love, and critically important reminders that there is more to life than work.

I'm incredibly lucky to have a wonderful and loving family, who have provided me with the opportunity to embark on this journey and supported me through it. Thank you to the editors: Noa and Dame, and to the production manager, Sandy. Thank you to Jef, Sonia and Daryl for their wisdom, interest and enthusiasm.

Gabriel Abrahams
November, 2021

Abstract

In recent decades, solid-state spin defects have emerged as systems whose quantum properties can be directly controlled and probed, potentially unlocking exciting applications as the fundamental building blocks of quantum computers and advanced sensors. These ‘quantum sensors’ are not theoretical, they are in the lab today, being used to probe everything from quantum-critical ‘Dirac’ fluids in 2D materials to imaging bio-magnetic structures in living cells. Compared with other sensors, quantum sensors are calibration-free, and in certain conditions provide a better trade-off between resolution, operating temperature, and sensitivity than other techniques. Here, we focus on sensing performed at room temperature and standard pressure. To date, the defect of choice for quantum sensing has been the nitrogen-vacancy (NV^-) centre in diamond, first utilised as a sensor in 2008. The NV^- centre is used for sensing temperature, electric and magnetic field vector, and strain. However, the NV^- is not without competition. Temperature and magnetic field sensing has been demonstrated using defects in silicon carbide (SiC), which has the advantage that SiC is industrially established compared with diamond. On the other hand, it has worse resolution and sensitivity compared with NV. In 2020, temperature, strain, and magnetic field sensing were demonstrated with the boron vacancy V_B^- in hexagonal boron nitride (hBN). As the discovery of spin-defects in hBN is so recent, there remain many details of its sensing capabilities still to be characterised. However, it has greater temperature sensitivity than the NV, and may offer a higher spatial resolution for widefield sensing. Unlike diamond and SiC, hBN is a van der Waals (vdW) material which may give it a unique advantage in sensing other vdW materials, by incorporating it into hetero-structures. Additionally, hBN is already established as a useful protection and enhancement layer in condensed matter studies of 2D materials such as graphene. Thus it is already primed for adoption provided its sensing capabilities can be further demonstrated.

The experiments described in this thesis employ a particular quantum sensing modality called “widefield quantum microscopy”, an analogy with optical widefield microscopes. Widefield quantum microscopes capture scalar (e.g. temperature) and vector (e.g. magnetic) fields over a two-dimensional surface, by imaging an ensemble of defects with a camera. This is in contrast with single defect sensing (which may be scanned to build up a 2D image) or single pixel sensing (where the detector has no spatial resolution). Although an established technique, widefield NV^- sensing remains challenging, in part due to its resolution being highly dependent on the quality of the diamond-sample interface. Chapter 2 presents a widefield NV^- microscope built and tested over November 2020 - September 2021, which implements a novel widefield probe design to overcome that problem. Alternatively, hBN may not face this interfacing problem, due to the thinness and flexibility of hBN sheets. Chapter 3 explores the feasibility of hBN as a widefield quantum sensor, presenting world-first results of widefield imaging with hBN, carried out from July - October 2021. Finally, Chapter 4 presents an application of widefield quantum sensing, demonstrating its ability to image photo-induced internal current flow in photovoltaic cells and capture the dynamic internal cell response. In support of these experiments, I constructed and operated a laser beam induced current (LBIC) mapping device between June - August 2020, and modelled the cell response using simulations throughout 2020-21, which helped mitigate the impact of reduced lab access due to COVID-19.

The fundamental laws of physics (quantum mechanics) at readily accessible length, temperature and pressure scales are well established. But the emergent laws of physics describing quasi-atomic systems (NV^- , V_B^- , ...) existing in quasi-worlds (diamond, hBN, graphene, ...) offer vast new landscapes for scientific discovery and societal benefit. This thesis presents a glimpse into the experimental and design techniques being utilised globally to unlock that potential.

Contents

1	Introduction to Spin Defect based Quantum Microscopy	2
1.1	The NV ⁻ defect in diamond	3
1.2	Widefield Quantum Microscopy	8
1.3	Scope of this thesis	9
2	Realisation of a Practical Diamond Nitrogen-Vacancy Widefield Microscope	10
2.1	Motivation and Concept	10
2.2	Implementation	10
2.3	Tests and results	14
3	Demonstration of Widefield Imaging of Spin Defects in Hexagonal Boron Nitride	27
3.1	Introduction	27
3.2	Properties of the V _B ⁻ in hBN	28
3.3	Methods	29
3.4	Preliminary results	32
3.5	Outlook	34
4	Application of Widefield Quantum Microscopy to Imaging Photocurrents in Photo-voltaic Devices	36
4.1	Principles of Current Mapping with NV	36
4.2	Theory of Photovoltaic Cells	37
4.3	Implementation of a Light Beam Induced Current Mapping Device	37
4.4	Computational Modelling	38
4.5	Spatio-temporal Electric Current Imaging with NV	40
4.6	Outlook	43
Conclusion		44
References		45

Chapter 1

Introduction to Spin Defect based Quantum Microscopy

Condensed matter studies have, in recent decades, revealed defects in solid-state crystalline materials that form quasi-atomic systems with properties well suited to study and application. In particular, such systems have applications as qubits in quantum computers, and as quantum sensors in the near term in next generation laboratory and potentially industrial settings [1–5]. This thesis focus on their role as quantum sensors. Broadly speaking, quantum sensors feature an overall spin that is susceptible to optical, magnetic, electric and strain induced effects. Such effects can be controlled to manipulate the spin, or emanate from a sample or device under examination. The spin state can be measured optically, using equipment found in a standard optics laboratory. Because measurements directly probe the quantum state of the sensor, quantum sensors are said to be ‘calibration free’ in contrast with classical sensors. Experimental conditions range from cryogenic [6, 7] to high temperature [8], and high pressure [9–11]. All sensors face a trade-off between spatial resolution, operating conditions, sensitivity and practicality. Thanks to their high sensitivity and spatial resolution over a wide range of operating conditions, achieved with relatively simple apparatus, there are certain situations where quantum sensors emerge as the optimal choice compared with alternative sensor technologies. This thesis focuses on room-temperature and standard pressure, which is suitable for studying technologies expected to operate in everyday environments, and biological behaviour such as cell dynamics [2] under ‘natural’ conditions. It is possible to address single defects, or ensembles of defects. Here, we concentrate on the “widefield” sensing modality, which simultaneously captures a spatially resolved 2D image of the fields (temperature, magnetic, electric...) of interest [5, 12]. Widefield microscopy involves addressing an ensemble of defects situated in a layer within the host material. The fluorescence (also commonly referred to as photo-luminescence, or PL) of the defects (which holds the spin information) is imaged onto a camera. In principle, each pixel of the image contains data corresponding to a diffraction limited spatial location. In practice, there may be complications due to optical scattering [13], however spatial correlation is maintained. Alternatives to widefield microscopy are single pixel (in which the image is effectively averaged) which lacks spatial resolution, or scanning microscopy. Both can be performed either using a single defect, or an ensemble (increasing sensitivity at the cost of resolution). Overall, scanning microscopy offers highest sensitivity and spatial resolution, at the cost of significantly increased complexity. Thus for samples where variations occur on scales of hundreds of nanometres or more, widefield microscopy can be the optimal choice.

Since 2008, the nitrogen-vacancy (NV^-) defect (or centre) in diamond has been the leading contender amongst optically addressable defects for quantum sensing [14–17]. The most notable alternative material hosting defects suitable for sensing is silicon carbide (SiC) [18]. Compared to diamond, industrial production silicon carbide is highly mature, making it favourable in terms of manufacturing. However, thus far defects in SiC do not perform as well as the NV^- in diamond [19] and have seen limited adoption. Recently (2020), the negative boron-vacancy (V_B^-) in hexagonal boron nitride (hBN) has emerged as an alternative defect with quantum sensing capabilities [20]. Compared to diamond or SiC, hBN is a van der Waals (vdW) material, and thus it can be exfoliated to atomically thin, flexible layers [21]. Additionally, it can be combined with other vdW materials of interest in tightly stacked heterostructures [22]. These features suggest the possibility that hBN may reduce the sensor-sample standoff from hundreds of nanometres with bulk diamond (or SiC) down to nanometres, resulting in greatly improved spatial resolution. Additionally, in studies of 2D materials, hBN is already well established as an insulation and passivation layer [23], thus primed to be augmented with sensing capabilities.

This chapter aims to provide a sufficient theoretical framework for understanding the operational principles of quantum widefield microscopy. Starting with the physics of the defect, the fundamentals of quantum sensing are addressed, and linked to the experimental parameters available for optimisation tuning. Chapter 2 presents the design, construction and test of a novel widefield NV⁻ microscope, addressing the challenge of interfacing diamond and sample to improve spatial resolution. Chapter 3 presents world-first widefield experiments with the V_B⁻ in hBN, extending the single pixel results reported by Gottscholl et al. [24] in 2021. Chapter 4 returns to NV⁻ microscopy, demonstrating a novel application to photocurrent sensing in solar cell devices, for device characterisation and optimisation. In this introduction, we focus on the NV⁻ centre, as relevant for Chapters 2 and 4. The spin-physics of the V_B⁻ defect is remarkably similar to the NV, as are the broad concepts of the photo-physics. Here, brief comparisons between the NV⁻ and V_B⁻ are made to highlight their different performance. Thus this introduction is also a useful guide for Chapter 3, which additionally includes a detailed introduction to the realisation of hBN as a quantum sensor.

1.1 The NV⁻ defect in diamond

The nitrogen-vacancy (NV) centre in diamond has been studied since the 1960s [25], coming into prominence as a magnetic field sensor circa 2008 [14, 15]. Magnetic resonance imaging using the negatively charged NV⁻ centre has proven to be a valuable technique for studying the magnetic and electronic properties of samples and devices [16, 17]. Widefield NV⁻ microscopy involves addressing an ensemble of NVs residing in a thin ($\lesssim 10 \mu\text{m}$) layer within the diamond, whose spin states are read out via their optically detected magnetic resonance (ODMR) spectrum onto a camera to map the stray magnetic field of a proximal sample [5, 12, 26]. This technique has found utility in imaging a wide ranging array of devices [27–35], as well as biological [36–39] and geological [13, 40, 41] samples. While widefield NV⁻ imaging has been demonstrated to have a range of applications, a number of challenges remain to be addressed for its capabilities to be fully realised by the broader scientific community. One example is the “interfacing” challenge. Briefly, to attain the highest spatial resolution, the NV⁻ defects must be in as close proximity to the magnetic sample as possible, thus interfacing the diamond and sample with precision is important. A practical approach to minimising standoff is presented in Chapter 2.

1.1.1 Electronic structure

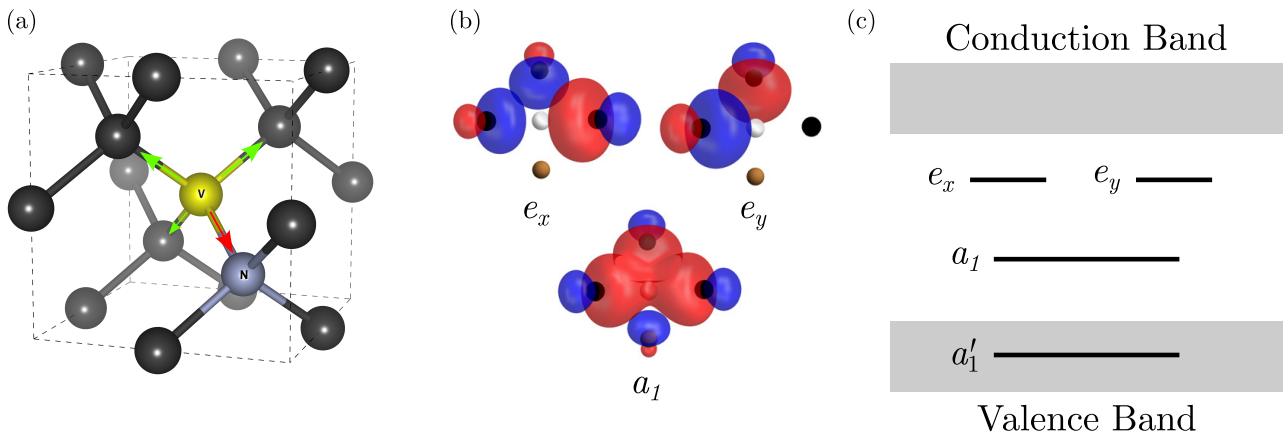


Figure 1.1: (a) A single NV⁻ defect in carbon diamond. Red arrow indicates the pictured NV⁻ defect axis. Green arrows indicate the other possible crystal axes. (b) Molecular orbitals (MOs) of the NV⁻ defect. Spheres indicate atomic sites: carbon is black, nitrogen is orange, vacancy is white. Red and blue components represent positive and negative contributions to the MOs respectively. (c) Energy levels of the MOs in (b) (neglecting strain). Panels (b) and (c) adapted from Ref. [42].

The electronic structure of the NV⁻ defect can be understood by considering its atomic structure. The defect is embedded in a diamond cubic carbon lattice. It is composed of a carbon vacancy and nearest

neighbour nitrogen atom, resulting in a point defect with C_{3v} symmetry. There are four possible crystal axes along which the defect can be oriented [Fig. 1.1 (a)], which enables 3D vector measurements, by simultaneously measuring up to 4 projections of vector fields. The centre forms an atom-like system, with energy levels existing between the valence and conduction band of the diamond matrix. Around the vacancy there are four dangling bonds (3 carbon + 1 nitrogen), resulting in 4 electrons. Nitrogen has a valency of 5 (1 more than carbon) donating an additional electron. The resulting system (5 electrons) is charge neutral and labelled NV^0 . Additionally, the defect may lose an electron resulting in the charge state NV^+ . Alternatively, an additional electron may be donated to the defect, for instance as a result of a substitutional nitrogen elsewhere in the diamond, resulting in a 6 electron system, the negatively charged NV^- . As will be discussed, it is the NV^- defect which has optical and spin properties leading to its versatility as a temperature, strain, magnetic and electric field sensor. Hence charge state conversion from NV^- to NV^0 or NV^+ is typically seen as undesirable [43]. This effect was seen in Section 2.2.4.2. Interestingly, this sensitivity to charge can be exploited for charge sensing, for example of biologically relevant electrochemical potentials [44]. In this thesis the focus is entirely on the NV^- defect.

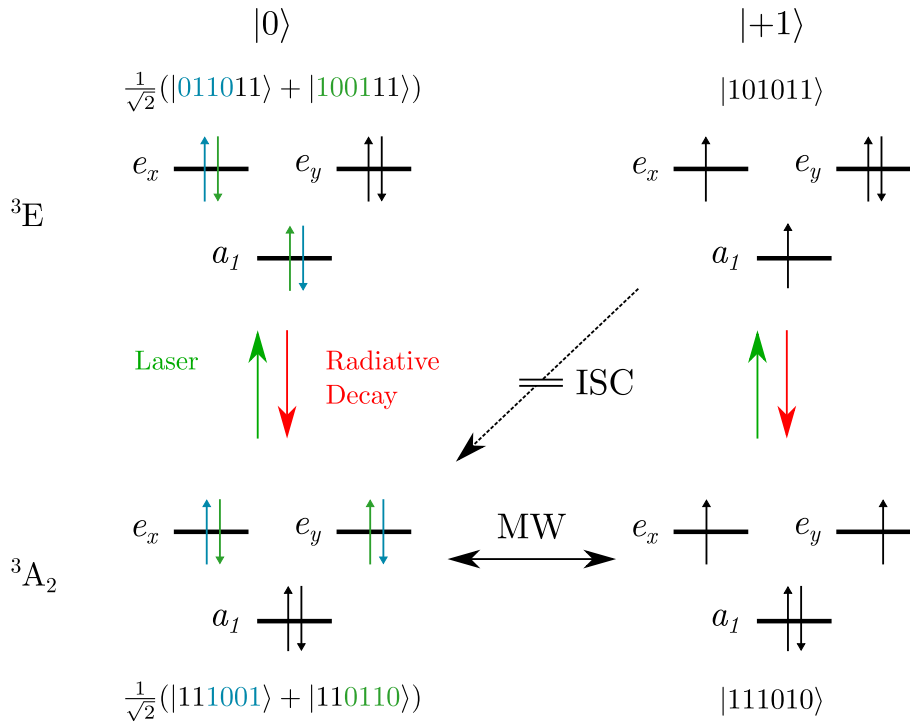


Figure 1.2: A representative depiction of the configuration states of the triplet ground state 3A_2 and triplet excited state 3E . Although the NV^- is a 6-electron system, the a'_1 MO is always filled, hence not shown here. The $|0\rangle$ and $|+1\rangle$ states are the $m_s = 0$ and $m_s = +1$ spin projections along the NV^- defect axis respectively. For simplicity, the $| -1 \rangle$ states are not shown. The Slater determinants of the configuration states are written with notation $|a_1\bar{a}_1e_x\bar{e}_xe_y\bar{e}_y\rangle$ where overbar denotes spin-down. MW denotes microwave driven spin transition in the ground state. The non-radiative decay path via a spin-selective inter-system crossing (ISC) is depicted with a dashed line, with intermediate singlet levels 1E and 1A_1 omitted. For a complete list of configuration and spin-orbit states, see [42]. Note that this diagram depicts only configuration states, neglecting spin-orbit interactions.

The electronic states in the NV^- are highly localised to the vacancy, justifying a molecular orbital approach to determining the energy levels [42]. Linear combination of atomic orbitals (LCAO), under the adiabatic approximation and neglecting hyperfine interactions may be employed to determine the molecular orbitals (MOs) of the spin system [Fig. 1.1 (b) and (c)]. From the MOs, the configuration states can be constructed. Using group theory, each energy level is labelled by its associated irreducible representation of the C_{3v} point symmetry group (E , A_1 and A_2). Detailed *ab initio* investigations have successfully predicted the precise energy structure in good agreement with empirical results, thus the NV^- defect may be considered well understood (in contrast with the V_B^- in hBN).

In Fig. 1.2, a selection of states are depicted to demonstrate how the electronic structure enables spin control and readout of the NV⁻ system. The ground state 3A_2 and excited state 3E are both spin triplets. The NV⁻ axis is the spin quantisation axis, with sub-levels $|m_s = 0\rangle_\alpha \equiv |0\rangle_\alpha$ and $|m_s = \pm 1\rangle_\alpha \equiv |\pm 1\rangle_\alpha$ where $\alpha = g(e)$ labels the ground (excited) state manifold. Application of a resonant microwave field can be used to drive the system in the ground state from $|0\rangle_g$ to $|\pm 1\rangle_g$.

Optical pumping (typically with a 532 nm laser) excites the system, which can then relax either via radiative decay or non-radiative decay. The latter involves a spin (projection) selective inter-system crossing (ISC) from the excited $|\pm 1\rangle_e$ states to the ground $|0\rangle_g$ state. Because of this spin-dependent fluorescence, the spin projection of the NV⁻ defect can be measured using ODMR spectroscopy.

The existence of the ISC also enables spin-polarisation, whereby optical pumping converts a system from the thermodynamic mixed state (in which $|0\rangle_g$ and $|\pm 1\rangle_g$ are equally probable) to a $|0\rangle_g$ polarised state, with polarisation reported $\sim 80\%$ [45].

To summarise, the fundamental mechanism of ODMR is as follows. First, the system initialised into the $|0\rangle_g$ state using optically induced spin polarisation. Next, a microwave field is applied, and if it is on resonance it will drive the $|0\rangle_g \leftrightarrow |\pm 1\rangle_g$ transition. Finally, the system is optically pumped from $|0\rangle_g, |\pm 1\rangle_g \rightarrow |0\rangle_e, |\pm 1\rangle_e$ and the spin dependent decay fluorescence is measured. This procedure is repeated with the microwave frequency swept through a spectrum, so that the resonant frequencies are observed as a dip in PL due to the non-radiative ISC.

1.1.2 Photo-dynamics

The photo-dynamics of the system are described by the transition rates or lifetimes of each state. The relevant exit transition rates Γ_i are depicted in Fig. 1.3. The excited states have lifetimes $1/\Gamma_1 \approx 12$ ns and $1/\Gamma_2 \approx 8$ ns in bulk diamond [45], suggesting spin-polarisation laser excitation should last hundreds of nanoseconds for multiple pump cycles to occur. The fluorescence lifetime (lifetime of the excited state) is thus at best 12 ns, which places a limit on the collection rate of photons (~ 100 MHz) and hence the integration time required to achieve a sufficient signal to noise ratio (SNR). The ISC 1E state is very short-lived with $1/\Gamma_3 \lesssim 1$ ns. However, $1/\Gamma_4 \approx 200$ ns at room temperature [46], indicating 1A_1 is a meta-stable state. Therefore the polarisation-rate is actually limited by $1/\Gamma_4$, in practice requiring microseconds per cycle. The depolarisation time T_1 is the decay rate for the transition from a polarised state (e.g. $|0\rangle_g$) back to a thermal mixed state. Thus for ODMR, the excitation intensity must ensure the photon absorption rate is greater than $1/T_1$, i.e. that a photon drives the NV⁻ to the excited state while its spin still contains information about the external magnetic field (or temperature, or strain). The NV⁻ is remarkably stable, with $T_1 \approx 6$ ms at room temperature, and up to minutes at low temperature [47]. In contrast, the V_B^- in hBN has $T_1 \approx 10\ \mu s$ at room temperature [48].

1.1.3 Magnetic field dependence

The sensing applications of the NV⁻ defect (temperature, strain, magnetic field) are all possible because each of these influences either lifts a degeneracy or causes an overall shift in the energies of the $|\pm 1\rangle_g$ spin states. This changes the resonant frequency at which microwave absorption occurs, hence is detected in the ODMR spectrum as separated dips in the PL at the corresponding frequencies [Fig. 1.3 (c)]. We first address these energy shifts, then describe microwave driving in more detail. The energy levels are captured in the ground state spin Hamiltonian, neglecting hyperfine (spin-orbit) interactions [16]. It is useful to split the Hamiltonian into three parts, along the defect axis (defined to be the z -axis) and perpendicular to it (x, y -axes):

$$\mathcal{H}_g = \overbrace{hDS_z^2 + g\mu_B B_{NV}S_z}^{\mathcal{H}_{||}} + \overbrace{g\mu_B(B_xS_x + B_yS_y)}^{\mathcal{H}_{\perp}} + hE(S_x^2 - S_y^2), \quad (1.1)$$

where h is Planck's constant, D and E are zero-field splitting parameters, $B_{NV} = B_z$ is the projection of \mathbf{B} along the defect axis, S_x, S_y and S_z are the spin operators, g is the Landè factor (≈ 2) and μ_B is

the Bohr magneton. For the NV^- at room temperature, $D \approx 2.87\text{GHz}$. E is strain dependent, with $E \ll D$. By aligning a strong bias field along the defect axis (as done in all chapters) we generally select the weak-field regime in which $\mathcal{H}_\perp \ll \mathcal{H}_\parallel$. In some cases the bias field is not well aligned, and off-axis effects are visible. For example, in Chapter 2, we focus only on magnetic field sensing, however strain does cause some modulation of the signal (e.g. due to different crystal sectors), which is seen in some images. Nevertheless, assuming the weak-field regime and neglecting strain, the resonant frequencies $f_{1,2}$ corresponding to the eigenenergies of the $|\pm 1\rangle_g$ states are:

$$f_{1,2} = D \pm \frac{g\mu_B}{h}|B_{\text{NV}}|, \quad (1.2)$$

which quantifies the frequency locations of the PL dips described earlier.

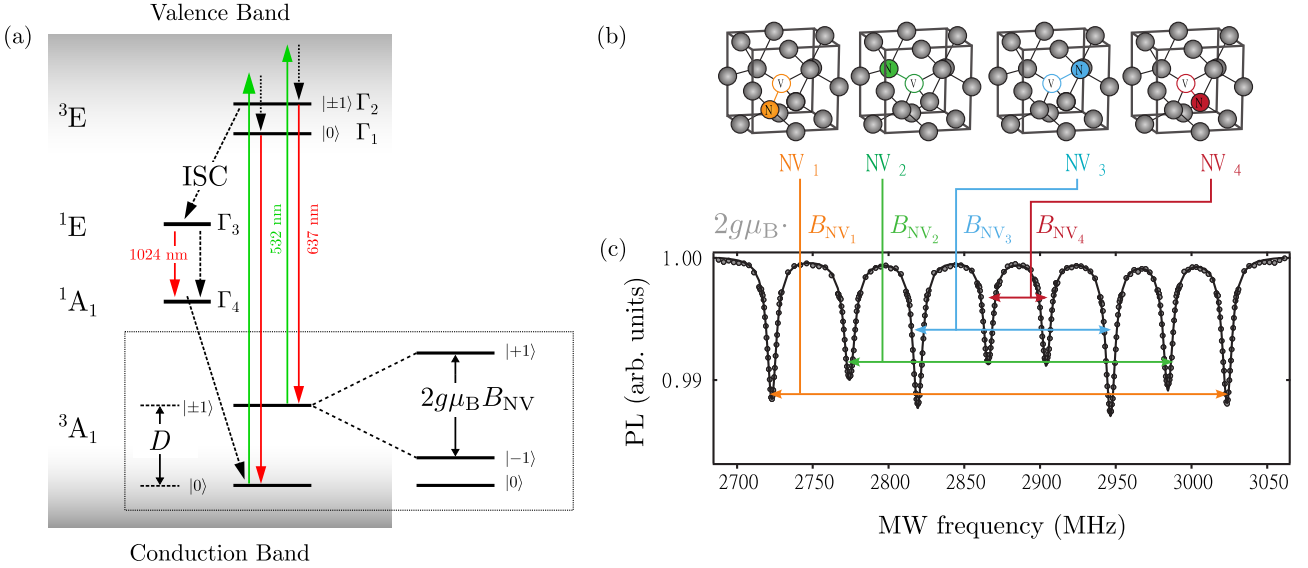


Figure 1.3: (a) Energy levels of the NV^- defect. Phonon-assisted 532 nm excitation to ^3E results in direct radiative decay and ISC enabled non-radiative decay. Dotted box indicates ground state splitting due to an applied magnetic field. (b) The four possible configurations of the NV^- along the crystallographic axes. (c) ODMR spectrum resulting from imaging an ensemble of NV^- defects, where the bias magnet is oriented such that there is a field component along each projection. The field direction is most aligned with the NV_4 axis, as indicated by the ODMR splitting. Panels (b) and (c) adapted from [5].

1.1.4 Spin dynamics

The ODMR response of a single defect is well represented by the intensity function

$$\mathcal{I} = \mathcal{R} [1 - \mathcal{C}\mathcal{F}(\omega)], \quad (1.3)$$

where \mathcal{R} is the photon detection rate and \mathcal{C} is the ODMR contrast associated with the dip in PL intensity, ω is the swept microwave frequency, and \mathcal{F} is the ODMR lineshape. It can be shown that \mathcal{C} increases with increasing microwave power [49]. The lineshape \mathcal{F} can be approximately described by the convolution of three independent response functions:

$$\mathcal{F}(\omega) = R(\omega) \circledast I(\omega) \circledast E(\omega), \quad (1.4)$$

where R , I and E are the resonance, instrument and environment response functions respectively (defined below).

The shotnoise limited magnetic field sensitivity η_B of a measurement with Δt duration is related to the minimum detectable magnetic field δB_{\min} through the relation

$$\eta_B = \delta B_{\min} \sqrt{\Delta t} \approx \mathcal{P}_{\mathcal{F}} \times \frac{h}{g\mu_B} \times \frac{\Delta I}{\mathcal{C}\sqrt{\mathcal{R}}}, \quad (1.5)$$

where $\mathcal{P}_{\mathcal{F}}$ is a line-shape dependent factor ≈ 0.77 when \mathcal{F} is Lorentzian and ΔI is the FWHM of the instrument response function. Thus maximising sensitivity is a multi-parameter optimisation problem [49]. Here we discuss briefly the shape of the response functions, initially neglecting optical effects.

The resonance response follows from Eq. 1.2, and is given by

$$R(\omega) = \sum_i \delta(\omega - \omega_i), \quad (1.6)$$

where ω_i are the resonant frequencies. Neglecting hyperfine interactions, there are simply two resonances ω_1 and ω_2 corresponding to $| -1 \rangle_g$ and $| +1 \rangle_g$ respectively.

The origin of the instrument response $I(\omega)$ arises from the microwave driven $| 0 \rangle_g \leftrightarrow | +1 \rangle_g$ transition (or equivalently $| 0 \rangle_g \leftrightarrow | -1 \rangle_g$). Consider a static magnetic field B_0 applied along the z -axis, and a microwave signal applied such that the magnetic component B_1 is along the x -axis. The time dependent Hamiltonian is then

$$\mathcal{H}_g = -\frac{1}{2}g\mu_B(B_0S_z + B_1 \cos(\omega t)S_x). \quad (1.7)$$

Making the rotating wave approximation and time-averaging, the state occupation probabilities are:

$$P(| 0 \rangle_g) = 1 - P(| +1 \rangle_g) \quad (1.8)$$

$$\text{and } P(| +1 \rangle_g) = \frac{\Omega_R^2}{\Omega_R^2 + (\omega - \omega_2)^2/4}, \quad (1.9)$$

where $\Omega_R \propto B_1$ is the Rabi frequency. The probabilities of occupying each state are directly proportional to the PL response in ODMR, hence $I(\omega) \propto P(| +1 \rangle_g)$. This is a Lorentzian line-shape with width $\propto \Omega_R$, hence we see that increasing the strength of the applied magnetic field results in an intrinsic broadening of the ODMR linewidth.

The environment response $E(\omega)$ is typically taken to be Lorentzian also, with full width at half maximum (FWHM) given by $1/T_2^*$ where T_2^* is the effective dephasing time. For a single defect, dephasing results in a broadening of the line-width because in practice, many measurements must be performed to integrate sufficient signal. In the case where the static bias field is aligned with the NV⁻ axis, dephasing is largely due to magnetic noise, when the bias field is off axis electric field noise due to strain dominates [50].

Practically, optically induced broadening can usually be neglected, thus is not discussed in detail here. The ODMR contrast \mathcal{C} decreases slowly with increasing laser intensity, while the response line-width increases linearly with laser intensity [49] up to saturation.

1.1.5 Tuning ODMR parameters

Using the basic theoretical framework established, we can now address how the experimental parameters can be tuned to roughly optimise magnetic sensitivity (compared with the multi-parameter optimisation of [49]). In Chapters 2 and 3 the sensing protocol used is continuous-wave (CW) ODMR, meaning the laser is always on, and the microwave is effectively on for the entire exposure (PL collection) period at each frequency. This is because the probed magnetic fields are both large (not requiring especially high sensitivity) and static (not requiring temporal resolution). More complex pulse sequences can be designed to reduce the effective T_2^* (improving sensitivity) and probe the dynamics of the applied magnetic field, as in Chapter 4. There is a trade-off in setting the strength of the microwave field, between increasing contrast (stronger field desired) and instrument response broadening (weaker field desired). The approximately optimal strength can be found by beginning with a low field strength, then increasing amplification (increasing contrast) until the line-width starts noticeably broadening. This method finds

the point where the overall line-width is no longer dominated by the environmental broadening. For example, see Section 3.3.2.

As mentioned above, in principle laser power can contribute to power broadening. However for the experiments in this thesis, the requirement that laser power is high enough for PL to be sufficiently above the background noise level overrides optically induced broadening concerns.

Quantum efficiency (QE) is defined in this context as the probability of the fluorescence path being taken when a decay event occurs. Multiplying the QE and the overall decay rate (inverse of the fluorescence lifetime) gives the radiative decay rate: how often a radiative decay transition occurs. Therefore the QE impacts the experimental dynamics, because it affects the Poisson rate of emitted photons given the laser intensity. The NV^- has a relatively high QE of ≈ 0.8 , and a sufficient fluorescence intensity is readily achievable with a $\sim 100\text{mW}$ laser beam focused to a $\sim 1\text{cm}^2$ spot size. In contrast, the V_B^- in hBN has very low QE of ~ 0.02 (see Sec. 3.2). This results in lower emission per excitation power, hence requires increased laser intensity to ensure the fluorescence signal is above the background noise levels of the camera.

In addition to parameter tuning, the ODMR signal quality can also be improved by normalisation with respect to a reference measurement. For CW ODMR, this is achieved by taking two PL images at each microwave frequency: first with the microwave off (reference), immediately followed with a measurement with the microwave field on (signal). Normalisation can be performed by division of the two measurements. The advantage of this approach is that random influences to overall PL on timescales longer than two camera exposures are effectively removed. Examples of such effects are charge state fluctuations across the ensemble, drift in the microwave or laser power applied, and drift in the camera sensitivity due to heating. In practice, such normalisation is almost always done, including in all ODMR measurements presented in this thesis. Reference normalisation can also be applied to pulsed sequences, as is described in Section 3.3.3.

1.2 Widefield Quantum Microscopy

As we have seen, spin defects such as the NV^- can be utilised as calibration-free probes of electric and magnetic fields, temperature and strain. It is possible to perform sensing using a single NV^- centre, for example embedded in a diamond tip, or an ensemble of NV^- centres, embedded in a larger diamond [51, 52]. A spatial map of the stray magnetic field (or other quantity) can be constructed either by scanning a single NV^- over a region (termed “scanning microscopy”) [Fig. 1.4 (a)] [51, 53–55], or by imaging an ensemble of defects arranged into a dense layer over the region of interest (termed “widefield microscopy”) [Fig. 1.4 (b)] [26, 56–58]. While scanning microscopy offers the highest resolution at tens of nanometres [59], it is technically complex compared with widefield, and cannot simultaneously image an area. In contrast, widefield microscopy has a diffraction limited spatial resolution of hundreds of nanometres, but is simpler to implement due to the absence of moving parts, and naturally performs simultaneous mapping. In circumstances where such resolution is sufficient, widefield microscopy can therefore be a desirable choice. There are a number of other techniques for magnetic field mapping, such as superconducting quantum interference devices (SQUIDs), Hall sensors, magnetic tunnel junctions and magnetic force microscopy (MFM). Considering the trade-offs between these approaches, NV^- sensing is most suited to sensing weak magnetic fields at cryogenic to room temperature environments due to its high sensitivity over a large temperature range, comparable spatial resolution and noninvasive sensing modality [5].

The spin dynamics for an ensemble of defects are similar to a single defect, with two main differences. Firstly, the sensitivity is improved by a factor $1/\sqrt{N}$, which follows from the increased photon emission rate of an ensemble, i.e. $\mathcal{R} \rightarrow N\mathcal{R}$ in Eq. 1.5. Secondly, T_2^* is re-interpreted as the *ensemble* dephasing time, where dephasing now happens in a single measurement of many defects, compared to a sequence of measurements of a single defect as described earlier. In the ensemble case, each defect experiences a

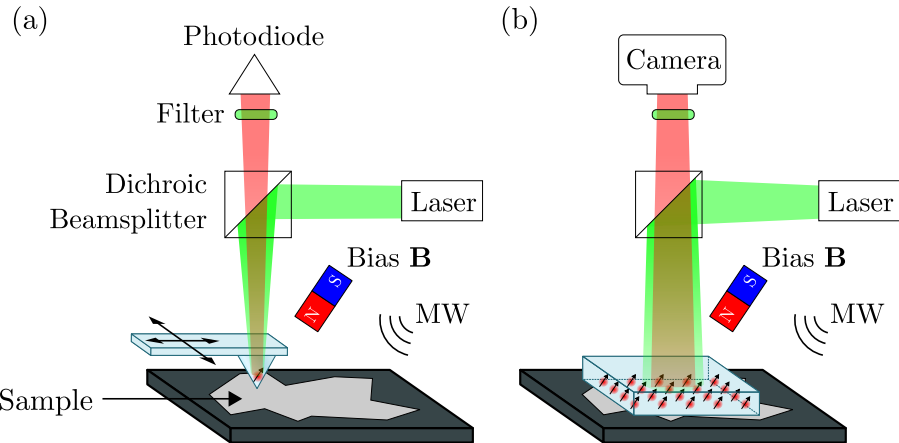


Figure 1.4: (a) Schematic of a scanning NV microscope. The diamond tip may host a single defect (as pictured) or an ensemble of defects. (b) Schematic of a widefield NV microscope.

different local magnetic environment, and hence has a different Larmor frequency. Thus if the ensemble average spin along the defect axis (z -axis) $\langle S_z \rangle$ initially polarised into some pure state were measured over time, it would decay to 0 (an even mix of $|0\rangle$, $| -1 \rangle$ and $| +1 \rangle$) at a rate T_2^* as the defects become increasingly out of phase with each other prior to each measurement. Note that as before, T_2^* is a phenomenological term, accounting for a number of effects which induce magnetic or electrical noise. These include intrinsic effects, such as coupling to electron spins in the lattice donated by substitutional N defects, variation in local environment (such as strain) due to crystal inhomogeneities, as well as extrinsic effects such as the non-zero spatial gradient of the bias magnetic field.

1.3 Scope of this thesis

For certain samples and experimental conditions, spin-defect widefield microscopy offers a competitive trade-off between sensitivity and operation over other sensing methods [5]. However, to fully realise the widefield microscope as a useful instrument in application areas such as experimental condensed matter physics, electronics, geology, biology and medical research requires overcoming operational challenges that currently impede its ease of use. Chapter 2 addresses the interfacing challenge faced by the NV in diamond, presenting a novel “widefield probe” solution and outlining further near term developments. Chapter 3 presents the emergence of the V_B^- in hBN as a candidate sensor for spin-defect widefield imaging, with potential advantages over current sensing technology (predominantly the NV in diamond). Finally, Chapter 4 illustrates the potential utility of quantum widefield microscopy, presenting its application to photocurrent mapping in solar cells.

Chapter 2

Realisation of a Practical Diamond Nitrogen-Vacancy Widesfield Microscope

The experimental work presented in this chapter was carried out between February 2021 - August 2021. Initially, the concept was to build a widefield microscope with angular control over the diamond (inspired by [60]), but without any particular optimisation method in mind. In the course of performing initial measurements, I noticed fringes in the fluorescence image moving in the same manner as when operating an optical profilometer (which I had recently been trained on by Dr. Nikolai Dotschuk). Highly detailed images such as 2.4 (d) followed. This work eventually led to a first-author manuscript recently submitted to Applied Physics Letters [61] which this chapter reproduces and expands upon.

2.1 Motivation and Concept

While greater spatial resolution is achievable using scanning NV⁻ microscopy, the parallel operation and high magnetic sensitivity of the widefield modality makes it well-suited to rapid, multi-purpose diagnostic imaging of magnetic materials and devices. However, its ease of use and potential for high-throughput imaging is often limited in practice by the requirement that the NV⁻ layer (and hence diamond sensor) be placed in close proximity with the sample. This is a challenge, as both the sensor and sample are relatively bulky objects (up to millimetres in size). Departures from flatness such as sample surface features or contaminants will cause misalignment between the diamond and sample surfaces resulting in standoffs which can significantly reduce image resolution. Broadly speaking, there are two ways to interface the diamond sensor with the sample [5]. In the first case, termed “sample-on-diamond”, the sample is fabricated directly onto the diamond. This method is ideal for minimising standoff, however it is impractical for measurements of many samples or for samples which cannot be fabricated in-house. In the second case, termed “diamond-on-sample”, the diamond sensor is independent from the sample, either placed on the sample or held in contact. This second method partly solves the practicality problem, but makes standoff minimisation more difficult. Here I present a widefield NV⁻ microscope with the flexibility of the “diamond-on-sample” method, while also demonstrating a systematic method for minimising standoff.

I followed the method demonstrated by Ernst et al. [60]. They reported the application of interferometry to scanning planar probe microscopy, showing that in situations involving a planar sensor parallel to a planar sample, the distance between probe and sample can be reliably minimised by first rotationally aligning the surfaces using interferometry as a feedback mechanism. They implemented this scheme for a 20 μm sized sample and millimetre-sized sensor, achieving $\approx 20 \text{ nm}$ standoff at the point of contact, allowing for nanometre-scale imaging through scanning. Here, I extend this concept to larger surface contact areas, as required for widefield imaging of large (millimetre to centimetre) scale samples. In the case of widefield imaging, a standoff of hundreds of nanometres is often sufficient to achieve near-optimum spatial resolution, relaxing the technical requirements. Therefore, I implemented a simplified and manual version of the alignment method which is suitable in this regime.

2.2 Implementation

2.2.1 Designing a Widefield Probe

The approach is based on a “widefield probe” which allows angular control of the diamond (the probe) with respect to the fixed sample [Fig. 2.1 (b)]. The widefield probe is constructed on a miniature printed circuit board (PCB) integrating a microwave loop antenna around a through hole (for imaging), and attached to a holding arm [Fig. 2.1 (d)]. The size of the loop and hole can be varied depending on the

application; all measurements here used a 3 mm hole diameter. A ~ 0.15 mm thick glass coverslip is glued over the through hole, and the diamond is adhered to the coverslip using low fluorescence glue. The arm is attached to a 5-axis stage: 2-axis rotation (rotation + goniometer) configured to allow angular adjustment of the diamond surface with minimal translation, and 3-axis linear motion for positioning and focusing. Finally, this probe stage is integrated into a compact (45×45 cm 2) footprint but otherwise standard widefield NV $^-$ microscope [Fig. 2.1 (f)]. Long working distance (≈ 1 cm) coverslip corrected objective lenses (10x NA = 0.3 and 20x NA = 0.45) are used to give sufficient clearance for the probe, as shown in [Fig. 2.4 (a)].

I designed the probe PCB in Altium CircuitMaker, they were manufactured by BEC Manufacturing. The design is quite simple, however required a couple iterations due to manufacturing constraints associated with through holes near routes (the antenna loop), and the small size of the probe. To overcome the size issue, the PCB ordered was larger than the probe, with the probe placed at the edge [Fig. 2.1 (c)]. I then cut the probe out using a Dremel rotary tool. To hold the probe, I selected 3mm copper rod, due to it being a non-magnetic, pliable material (for bending into shape) which could be easily soldered to the probe.

To glue the diamond (described below) to the probe I experimented with low fluorescence UV setting glue and also PMMA glue. The UV glue worked well, however was difficult to remove, and hence test different diamonds pieces. I trialled PMMA because it is low fluorescence and much easier to remove than UV glue, but found that it didn't form strong enough bonds between the diamond and probe, so the diamond would slip during the alignment procedure.

2.2.2 Microscope Hardware

The experimental setup is shown in Fig. 2.1. Continuous-wave (CW) laser excitation was produced by a $\lambda = 532$ nm solid-state laser outputting 1.5 W of power (Dragon Lasers FN series). The beam was attenuated to 300 mW, beam expanded (5x) and focused using a widefield lens ($f = 100$ mm) to the back aperture of the objective lens. I used two different objectives for magnetic imaging: (i) Nikon S Plan Fluor 20x ELWD, NA = 0.45, working distance 6.9-8.2mm; (ii) Nikon Plan Fluor 10x, NA = 0.3, working distance 16mm. The PL from the NV $^-$ layer was collected by the same objective, separated from the excitation light with a dichroic mirror, filtered using a longpass filter, and imaged using a tube lens ($f = 200$ mm) onto a CMOS camera (Basler acA2040-90um USB3 Mono).

Microwave excitation was provided by a signal generator (Windfreak SynthNV $^-$ Pro) gated using a switch (Mini-Circuits ZASWA-2-50DR+) and amplified (Mini-Circuits ZHL-16W-43+). The output of the amplifier is directly connected to the PCB of the widefield probe using a coaxial cable. A pulse pattern generator (SpinCore PulseBlasterESR-PRO 400 MHz) was used to gate the microwave and to synchronise the image acquisition. The microwave switch required an inverted logic signal, which I implemented by building a simple logic inverter circuit (using the Texas Instruments SN74S140N chip).

2.2.3 Pulse Sequence and Software

Although a LabView program implementing the quantum sensing protocols existed, I had to write a significant amount of new code to integrate the camera and signal generator, which were both acquisitions that operated differently to similar components used in previous setups.

Camera: Basler acA2040-90um

The camera has a large number of configurable options. Image acquisition can either be automatic, or triggered using an external source; the latter was used here. The exposure time of each frame can be fixed, automatic, or set by the duration between triggers (used here). The image resolution, spatial resolution (pixel binning), and bit depth (\log_2 number of grey scale values) can all be set. Initially I wrote a simple program to learn how to trigger the camera, and test how different settings affected the camera performance. Importantly, unlike previously used cameras, I found that after an exposure, a wait time

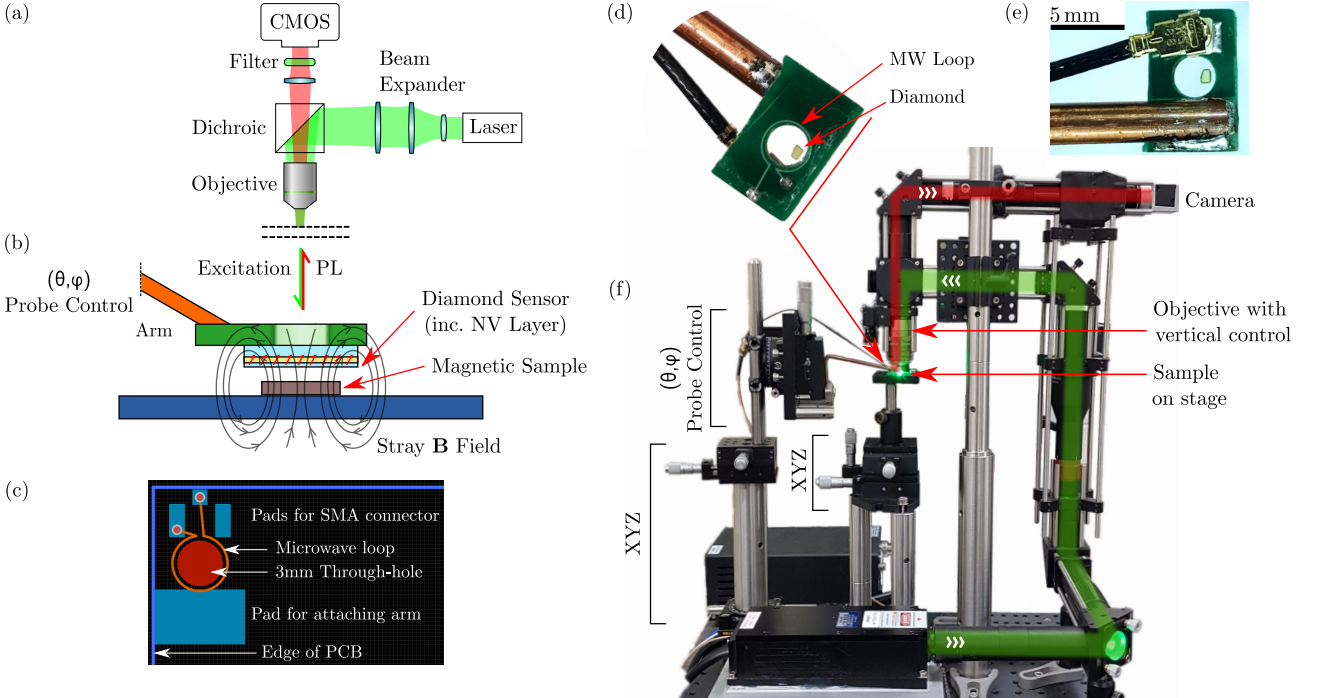


Figure 2.1: (a) Optical path of the microscope. Excitation path in green, epifluorescence path in red. CMOS (Complementary Metal-Oxide Semiconductor) denotes the camera sensor. (b) Schematic of the widefield probe concept. A diamond sensor attached to an arm is mechanically brought into alignment with the sample under study. The stray magnetic field is then imaged by the NV⁻ layer through its fluorescence (PL) response. (c) PCB design (one of many) which is sent to the manufacturer for fabrication. SMA (SubMiniature version A) denotes the microwave connection port. (d) Photograph of the probe, attached to the orientation control arm (copper) and a coaxial cable (black). A microwave (MW) loop antenna is imprinted onto the PCB. The diamond is glued to a glass coverslip, which is glued to the PCB. (e) Photograph of the probe from above. Diamond is visible in the right half of the thru-hole. (f) Photograph of the complete microscope. Green highlight: 532 nm excitation path. Red highlight: 650 – 750 nm PL path. The bias magnet, signal generator and microwave amplifier are not pictured, however all fit onto the breadboard shown.

dependant on the bit depth is required prior to the next exposure, otherwise the camera drops frames. This required wait is despite the camera having automatic image overlap acquisition, whereby the next exposure may be started before the previous readout is complete. For example, for 8 bit depth images the wait time must be $> 250 \mu\text{s}$, and for 12 bit depth it must be $> 4 \text{ ms}$. I also found that minimum exposure times can be very short (down to $\sim 1\text{ms}$) depending on resolution, which means very high frame rates are possible at the expense of field of view or spatial resolution. Upon integrating the camera and signal generator, this information was critical to ensuring timing synchronisation remained consistent throughout the pulse sequence.

Signal Generator: Windfreak SynthNV⁻ Pro

The SynthNV⁻ Pro is configured to perform a linear continuous frequency sweep by setting a fixed power, starting frequency, stopping frequency and step size. Frequency steps are triggered using the PulseBlaster. I also implemented a routine to program the SynthNV⁻ with a table of frequencies and power levels, allowing for arbitrary microwave sequences. Although not used in this work, this would allow for schemes such as Bayesian experiment design, which aims to minimise the number of frequencies scanned to establish the resonant frequencies [62]. The output microwave signal is independently gated using a switch, so that it is off during the reference image and on during the signal image.

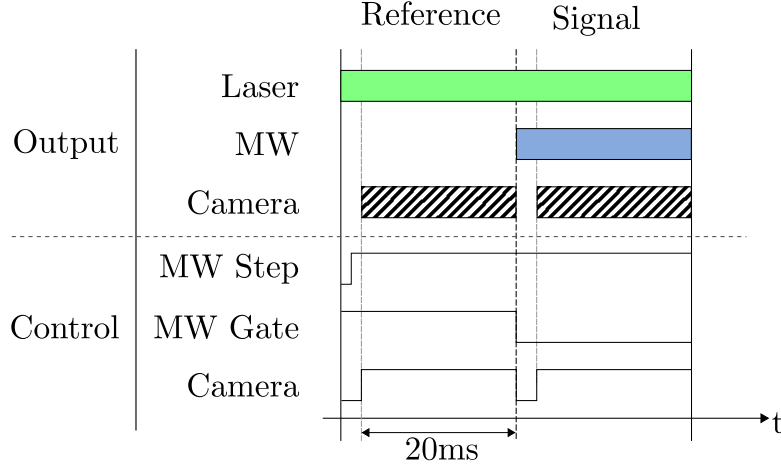


Figure 2.2: Timing diagram indicating the programmed signals (Control) and resulting system behaviour (Output). Camera blocks indicates time the camera is exposing.

2.2.4 Diamond sensor

The NV-diamond samples used in this work were made from $4\text{ mm} \times 4\text{ mm} \times 400\text{ }\mu\text{m}$ type-Ib, single-crystal diamond substrates grown by high-pressure, high-temperature (HPHT) synthesis, with $\{100\}$ -oriented polished faces, purchased from Chenguang Machinery & Electric Equipment. The diamonds featured multiple sectors with various levels of nitrogen content as inferred from the different shades of yellow [Fig. 2.3 (d)], but all sectors had very low level of NV^- PL initially.

2.2.4.1 Fabrication and implantation

Implantation was modelled and carried out by Brett Johnson and Qi Lim using Australian National University facilities, and subsequent processing (annealing and cleaning) was performed by Alex Healey at the University of Melbourne. The process is described briefly here. For further details see Healey et al. [63].

To form a dense NV^- layer near the surface, the diamonds were implanted with 4 MeV Sb ions with a dose of $3 \times 10^{11}\text{ ions/cm}^2$. A full cascade Stopping and Range of Ions in Matter (SRIM) Monte Carlo simulation was performed to estimate the depth distribution of the created vacancies [Fig. 2.3 (c)], predicting a distribution spanning the range 0 - 1100 nm with a peak vacancy density of $\sim 170\text{ ppm}$ at a depth of $\sim 800\text{ nm}$. Following implantation, the diamonds were annealed at $900\text{ }^\circ\text{C}$ for 4 hours in a vacuum of $\sim 10^{-5}\text{ Torr}$ to form the NV^- centers. After annealing, the plates were acid cleaned (30 minutes in a boiling mixture of sulphuric acid and sodium nitrate).

2.2.4.2 N concentration

I performed an initial characterisation of the diamond by taking ODMR images at different locations on the diamond. Surprisingly, the contrast varied drastically across the diamond: ranging from 0.4% - 4%. The contrast variation was loosely correlated with the colour of the diamond, and hence with the density of nitrogen: darker shade of yellow \iff high N concentration \iff lower contrast. Additionally, the contrast was sharply correlated with the NV^- PL: bright PL \iff high contrast \iff low N concentration. In fact this effect has been previously reported, and is understood to be due to high levels of nitrogen resulting in modification of the NV^- charge state via electron tunnelling [64]. The PL of the resulting charge state is likely quenched due to the addition of non-radiative decay pathways [65].

It is desirable to use high contrast regions only for sensing (as higher contrast \implies higher sensitivity), hence I proceeded to map the PL across multiple diamonds to determine the size of sectors with “good” (low) N concentrations. Because the diamonds are larger than the microscope field of view I created a simple PL acquisition and image stitching program in LabView, and used this to create the image in

Fig. 2.3 (e).

2.2.4.3 Laser Cutting

For alignment, it is desirable that the diamond probe be as small as possible: the smaller the diamond, the smaller the standoff variation across the probe for the same angle. Thus the contact diamond surface should be only be as large as the imaging field of view. I used a laser cutting system to cut a variety of probes from $4 \times 4 \text{ mm}^2$ diamonds, and test different cutting techniques for this and next generation probe designs. As this was the first time designing and implementing such a probe, the initial work I carried out using the laser cutter was exploratory.

After a failed initial cut (only 50% through the diamond), I established that because the diamond is $400 \mu\text{m}$ thick, the cutting laser needs to be refocused multiple (3 – 4) times throughout the cut. Test cuts are seen in Fig. 2.3 (a,b). To make the final probes, I used the PL map described above to cut sectors with low N concentration. The resulting diamonds are $< 1 \text{ mm}^2$ in size [Fig. 2.3 (g)]. For the magnetic sample studied in this work, the cut pieces described above were an appropriate size as the sample itself was $\sim 1 \text{ mm}^2$. However, in future we may study smaller devices, in which case it would be appropriate to reduce the area of the contact face of the diamond. As seen in Fig. 2.3 (a), I also experimented with smaller pieces, down to $0.25 \times 0.25 \text{ mm}^2$. Another possibility would be to cut a mesa, which could be done simply by cutting a larger piece, and then removing material only from the surface by appropriately focusing the laser (similar to the failed cuts). Possible advantages of the mesa designs are ease of handling and stability once attached to the probe.

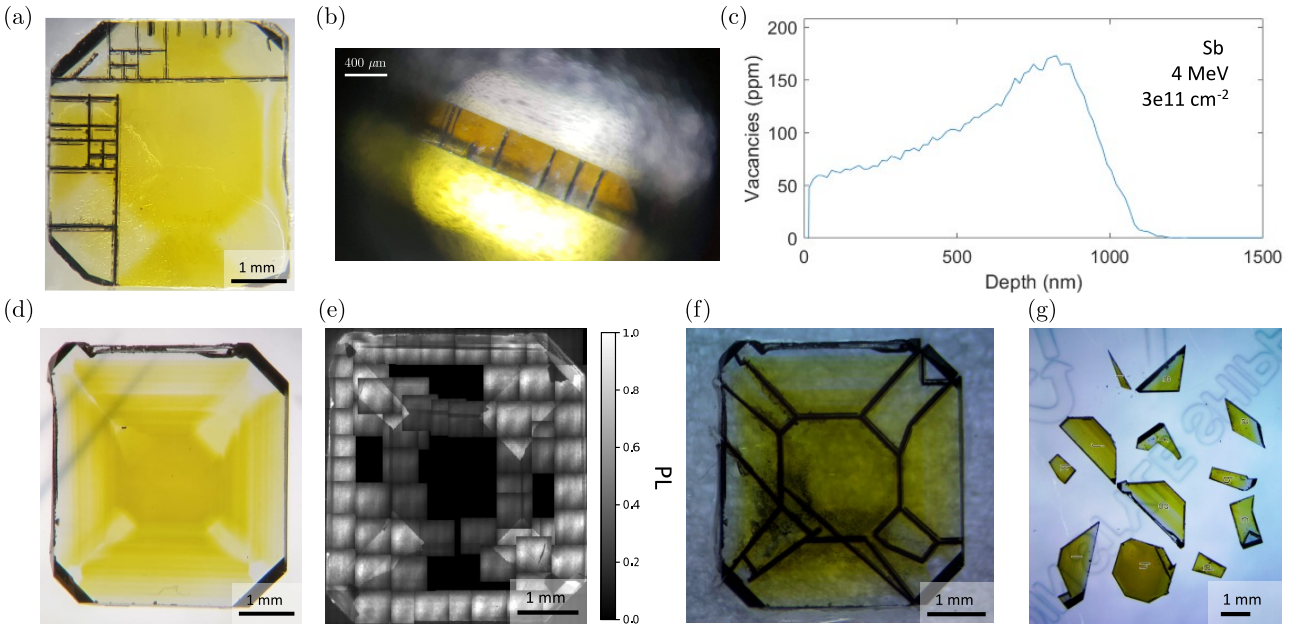


Figure 2.3: (a) Diamond with a number of test-cuts used to determine laser cutting parameters. (b) Side view of the diamond in (a), showing cuts that did (and didn't) go all the way through. (c) Stopping and Range of Ions in Matter (SRIM) simulation of the implantation used, showing the vacancy concentration as a function of depth. Assumed parameters are a diamond density of 3.51 g cm^{-3} and a displacement energy of 50 eV. (d) Photograph of the diamond used for sensing, as purchased. (e) Stitched PL map of the diamond shown in (a) after implantation and annealing. (f) Photograph of the same diamond after laser cutting. (g) Photograph of the resulting pieces after separation and acid cleaning.

2.3 Tests and results

To test the method and evaluate integrated system performance, I imaged an ultrathin film, millimetre-sized magnetic device fabricated on a Si/SiO₂ substrate [Fig. 2.4(b)]. This device was supplied by Vincent Jacques (University of Montpellier, France). The film is a W/CoFeB/MgO stack with a 1 nm thick CoFeB

layer exhibiting perpendicular magnetic anisotropy as reported by Gross et al. [66]. It is a patterned permanent magnet, with features such as pads and stripes ranging from $0.5 - 2 \mu\text{m}$ in width. When focusing the objective onto the sample surface with the diamond at some distance, the device structure is visible in the reflected NV^- PL [Fig. 2.4(c)]. An example resulting magnetic image obtained after alignment is shown in Fig. 2.4 (d). Below, I describe the critical steps that led to this image.

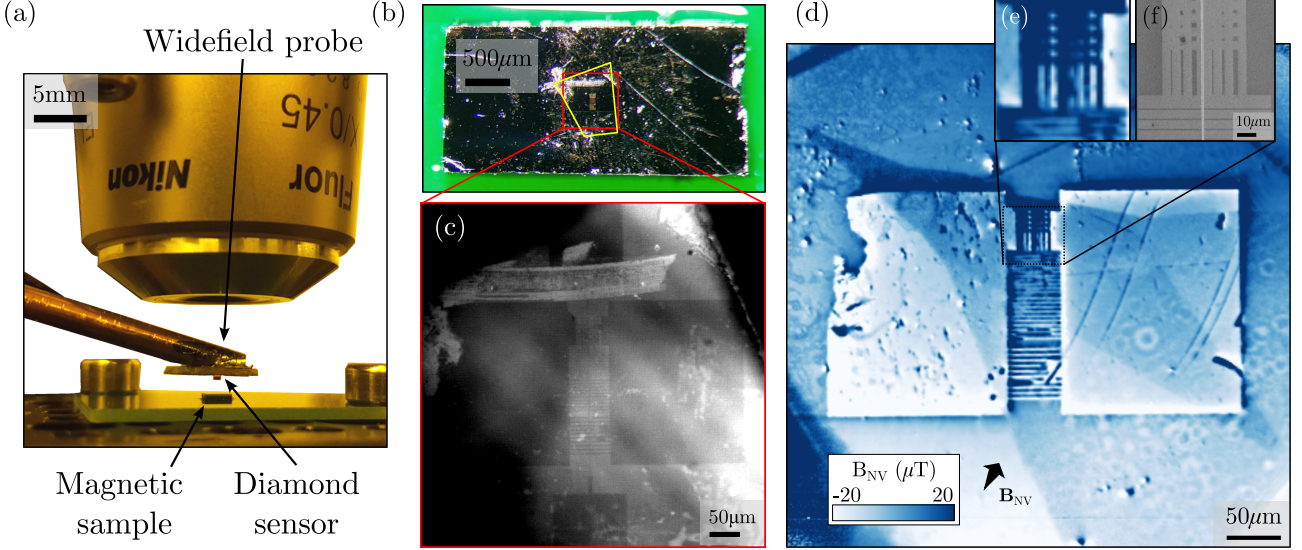


Figure 2.4: (a) Photograph of the widefield probe before being brought into contact with the sample. (b) Photograph of the sample, sitting atop a printed circuit board (PCB). Yellow outline indicates approximate diamond footprint. (c) Image of the sample using the reflected NV^- PL. The diamond is raised to be out of focus; its edges are clearly visible in the top left and top right of the image. The large dark pads on the left and right and the rungs connecting them correspond to the magnetic film, while the rest of the sample is the bare substrate. The smaller square pads on the top and bottom and the line connecting them are the remains of a gold stripline, not used in this experiment. (d) Magnetic map (B_{NV}) of the sample after alignment optimisation. The diamond position has been moved relative to image (c). The statistical (pixel to pixel) noise is about $1 \mu\text{T}$. I applied a 3-point plane subtraction to remove the bias magnetic field. Arrow indicates estimated NV^- axis direction. (e) Zoom in of the same magnetic image. (f) Scanning Electron Microscope (SEM) image corresponding to (e), showing the smallest device features (dots and vertical bars). From left column to right the features have smallest dimension $0.5, 1$ and $2 \mu\text{m}$ (repeated).

2.3.1 Magnetic imaging

The ODMR peaks $f_{1,2}$ are generally dependent on temperature, strain and magnetic field [67]. In the regime where the applied field along the NV^- axis is large compared to that perpendicular, $f_{1,2}$ are mostly dependent on magnetic field [16],

$$f_{1,2} = D \mp \gamma_e B_{\text{NV}}, \quad (2.1)$$

where $D = 2.87 \text{ GHz}$ is the zero field splitting, $\gamma_e = 28 \text{ GHz T}^{-1}$ is the gyromagnetic ratio and B_{NV} is the magnetic field projection along the NV^- axis.

In this aligned field regime, the magnetic field can then be deduced from the two ODMR frequencies,

$$B_{\text{NV}} = \frac{f_2 - f_1}{2\gamma_e}. \quad (2.2)$$

All B_{NV} maps were obtained in this way. Additionally, the zero-field splitting D can be obtained via

$$D = \frac{f_1 + f_2}{2}. \quad (2.3)$$

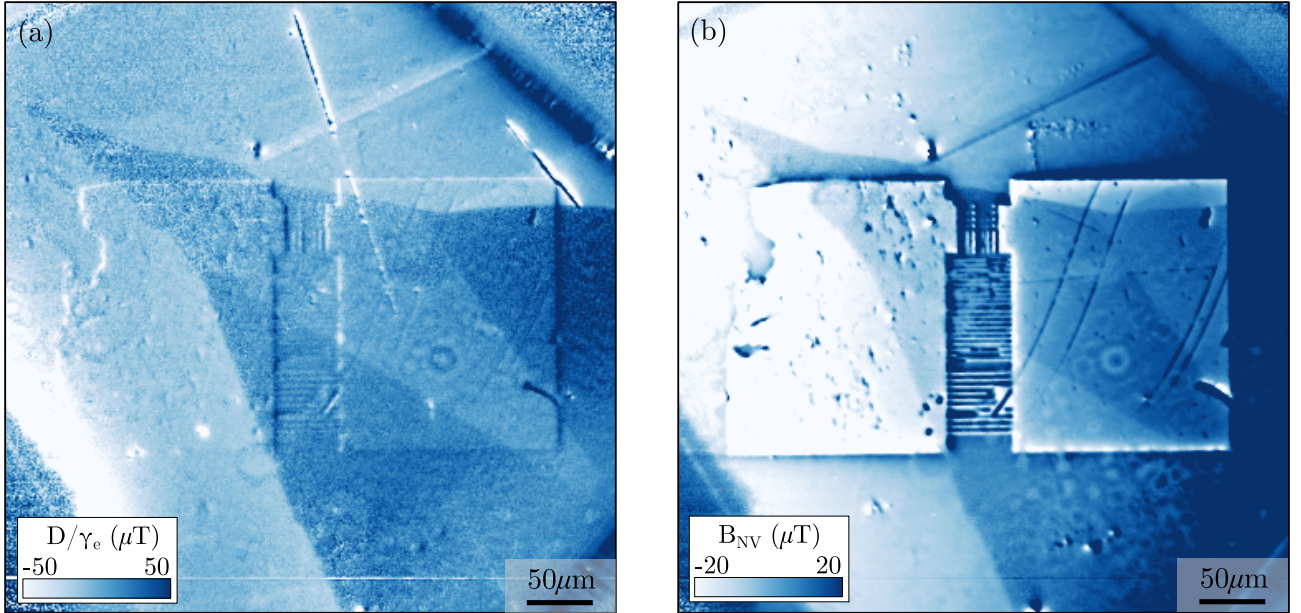


Figure 2.5: Images obtained from the same data that led to Fig. 2.4(d). (a) Map of the zero-field splitting parameter D deduced from Eq. 2.3. (b) Map of B_{NV} as deduced from Eq. 2.2, without 3-point plane subtraction.

The D map corresponding to the data in Fig. 2.4(d) is shown in Fig. 2.5. Large uniform sectors with different D values are visible, which match sectors with different levels of nitrogen content in the HPHT diamond. The variation in D between different sectors is attributed to differences in strain.

Comparing Fig. 2.5(b) (which is the same as Fig. 2.4(d) but without 3-point plane subtraction, and nominally representing B_{NV}) with Fig. 2.5(a) (nominally representing D), we notice some correlations: the strain sectors are visible in the B_{NV} map, whereas the magnetic devices are visible in the D map. This cross-talk is due to the fact that here the bias magnetic field was not well aligned with the NV^- axis. In the misaligned regime, Eq. 2.2 and 2.3 are only approximate relations [16], leading to an apparent cross-talk between the resulting maps. However, more accurate alignment or performing 8-peak ODMR (measuring all 4 NV^- orientation classes [68]) can reliably resolve this. For example, the magnetic images shown in Figs. 2.6 and 2.7 were obtained with a better bias field alignment, leading to significantly reduced strain-induced artefacts.

2.3.2 Alignment

The alignment procedure is as follows. As the diamond and sample are coarsely brought together, interference fringes due to an angular displacement become faintly visible in the PL image. The fringes are due to interference of the collimated 532 nm excitation beam between diamond and sample surface, resulting in patterned NV^- excitation and hence modulated PL [Fig. 2.6 (a,d)]. The fringe spacing corresponds to the relative angle between the sensor and sample surfaces: $\theta \approx \lambda/\Delta$ where θ is the angular displacement, λ is the excitation wavelength (532 nm) and Δ is the fringe spacing. Static PL images are shown in Fig. 2.6, before alignment (c) and after alignment (d). These are the PL images taken before bringing sample and diamond into contact for with the magnetic images in Fig. 2.6 (e) and (f) respectively. Adjusting the diamond angle causes the fringes to rotate and spread along the axis least aligned. Ideally, the fringes are ultimately spread such that only one band is visible. Orientation alignment is performed while there is a small air gap between the diamond and sample. Finally, the diamond and sample are brought into direct contact by further vertical adjustment. Contact is determined from the NV^- PL video feed. The NV^- layer is first moved into focus, then the sample is brought up until it is seen to contact the diamond (sample features come into focus, and the sample is stabilised when the diamond comes into contact).

The orientation alignment described above is similar to step 1 of the procedure (tilt correction) described by Ernst et al. [60]. Step 2 of that procedure is bringing the probe into contact using Piezo motor control, with the distance monitored via Brewster angle microscopy. I found manual translation sufficient to achieve comparable standoff with values reported in the literature, however the method described by Ernst et al. [60] is a useful guide to techniques for further reducing standoff, and automating the procedure, in a future implementation of the widefield probe.

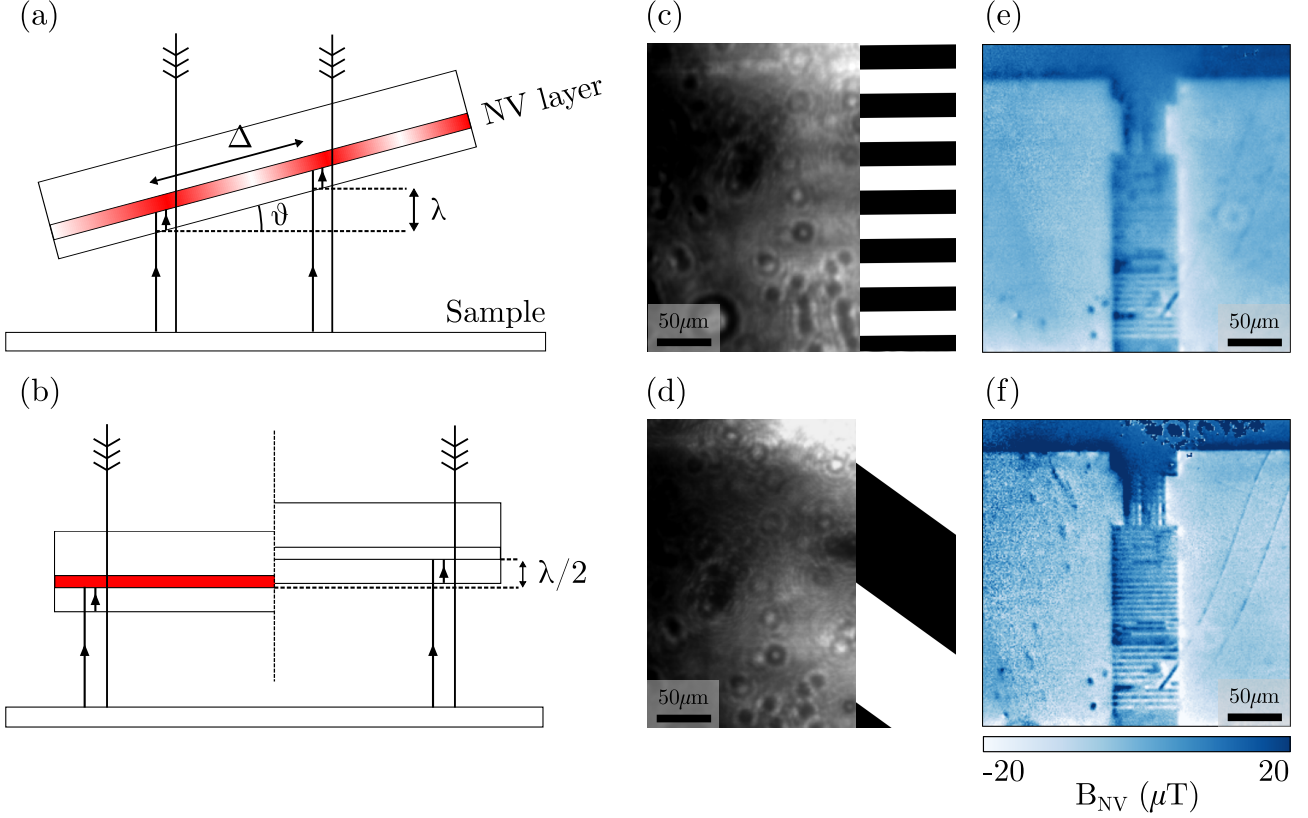


Figure 2.6: (a,b) Schematic of sensor-sample interfacing without (a) and with (b) angular alignment. On the left (right) side of (b) the diamond is shown at a distance where constructive (destructive) interference occurs. (c,d) Fluorescence images corresponding to (a,b) (left part is actual data, right part is a guide to the eye). As alignment is improved, gap between fringes increases. (e,f) Magnetic images corresponding to (c,d), respectively, showing a clear improvement in sharpness with the alignment step. A plane subtraction to remove the bias magnetic field has been performed.

After applying this alignment procedure, a magnetic image of the sample is acquired. An example magnetic image is shown in Fig. 2.4(d), which cleanly reveals device features in contrast with the comparatively dirty optical image, despite some residual imaging artefacts attributed to diamond features and off-axis bias field alignment (see Section 2.3.1). Note that in Fig. 2.4(d) the bias field of 3.6 mT was removed via a three-point plane subtraction. The resulting image was obtained using a 10x objective, providing a field of view (FOV) of 565 μm at 1024px \times 1024px resolution (pixel size 552 nm). Magnetic features such as the rungs were resolved after ~ 10 minutes of integration. To resolve micron-scale details required integration times on the order of hours. As seen in the zoom-in magnetic image and scanning electron microscope image [Fig. 2.4(e-f)], magnetic bars down to a width of 0.5 μm can be resolved. All resolved features are separated by $\approx 5 \mu\text{m}$ implying that the resolution is at or below 5 μm .

To illustrate the importance of the alignment step, images resulting from two different imaging conditions, obtained using a 20x objective, (hence, resulting in a smaller FOV compared to Fig. 2.4(d)) are shown in Fig. 2.6. In the first case, no angular alignment is performed [Fig. 2.6(a)], and tight fringes are visible in PL [Fig. 2.6(c)]. As a result, the magnetic image is blurry [Fig. 2.6(e)]. I found that forcing the

diamond into a closer contact without first performing alignment does not actually reduce the standoff, which can be understood by considering the schematic in Fig. 2.6(a), where the diamond contacts the sample at a point resulting in non-uniform standoff. I also “dropped” the diamond and took ODMR images (microwave provided by a PCB with no diamond), which produced similarly blurry magnetic images. This is likely due to either features on the sample surface or contaminants causing similar point like contact to above, resulting in the diamond resting at an angle. Dust particles have size on the order $1 - 100 \mu\text{m}$, thus easily able to cause significant standoff distances. In contrast, minimising the angle through monitoring the fringes before lowering the diamond reliably produced the sharpest images [Fig. 2.6(c,d)]. This is because the aligned diamond will overall be within close proximity with the sample. Alignment is maintained while contact is made, thus the aforementioned contact points may be forced away (i.e. contaminants) or otherwise only limit overall standoff to a small distance, rather than causing large standoff. The relative tilt between sensor and sample plane is determined by the fringe separation. The full PL FOV for the 10x objective is $1130 \mu\text{m} \times 1130 \mu\text{m}$ (this is cropped by a factor 2 for the magnetic image in Fig. 2.4(d)). Thus, once a single fringe is visible, the relative tilt between sensor and sample planes is within 0.47 mrad. This corresponds to $\sim 0.5 \mu\text{m}$ variation in standoff across the $\sim 1 \text{ mm}$ FOV. I found this precision to be sufficient for noticeable improvement compared to not performing alignment.

2.3.3 Resolution Estimation

Having demonstrated a reliable way to align the NV-sample interface, the factors affecting spatial resolution in the magnetic images were investigated. Firstly there are ‘optical’ effects such as diffraction, and also aberrations due to imaging through the diamond and coverslip. These effects limit the resolution in imaging the PL of the NV⁻ layer, independent of sample. There are ‘standoff’ effects, namely the fact that the stray magnetic field seen by the NV⁻ layer is a convolution of the sample’s magnetisation with a resolution function whose width is proportional to the NV-sample standoff d_{SO} [17, 69], as well as averaging over the finite thickness of the NV⁻ layer [70].

To estimate d_{SO} , I followed the method in Hingant et al. [71], analysing line-cuts over the edge of the large magnetic pads [Fig. 2.7(a-c)]. The model is given by the theoretical stray field at a free standoff d_{SO} , integrated over the NV⁻ layer thickness, and convolved with a Gaussian function of fixed width r_{opt} to capture optical effects. The other free parameters are the NV⁻ orientation [spherical coordinates (θ, ϕ)] and sample spontaneous magnetisation M_s . The assumed parameters are the film thickness ($t = 1 \text{ nm}$) and NV⁻ layer thickness, approximated to be $t_{NV} = 1 \mu\text{m}$ with a uniform distribution [Fig. 2.7(d)]. Although in principle the optical resolution may be worse (larger profile width) than the diffraction limit, I approximate them to be equal, which resulted in a good model fit. This leads to the estimated standoff d_{SO} being an upper bound for the actual standoff.

2.3.3.1 Magnetic field fitting

The magnetic field along a line-cut perpendicular to an infinite edge of a perpendicularly magnetised film (spontaneous magnetisation M_s , thickness t) at standoff distance d_{SO} is given by [71]:

$$B_x = \frac{\mu_0 M_s}{4\pi} \ln \left(\frac{x^2 + (d_{SO} + \frac{t}{2})^2}{x^2 + (d_{SO} - \frac{t}{2})^2} \right) \quad (2.4)$$

$$\text{and } B_z = \frac{\mu_0 M_s}{2\pi} \left[\arctan \left(\frac{x}{d_{SO} + \frac{t}{2}} \right) - \arctan \left(\frac{x}{d_{SO} - \frac{t}{2}} \right) \right], \quad (2.5)$$

where x is along the line-cut (film edge at $x = 0$) and z is normal to the magnet plane. The magnetic field projection along the NV⁻ axis is then

$$B_{NV} = \sin \theta \cos \phi B_x + \cos \theta B_z, \quad (2.6)$$

where (θ, ϕ) are the spherical angles characterising the NV⁻ axis direction.

Taking Eq. 2.4 to the thin film limit ($t \ll d_{SO}$) gives a Lorentzian profile, with a full width at half maximum (FWHM) equal to $2 \times d_{SO}$ [71]. This profile is the result of upwards continuation of the magnetic field from the sample plane (a delta function in this case for the B_x component) to the sensing (NV) plane [69]. Thus, one can view the Lorentzian of width $2d_{SO}$ as the point spread function (PSF) associated with the stray field measurement at a finite standoff, which is a helpful concept when discussing spatial resolution. In general, however, the PSF may differ depending on the type of magnetic field source and the field component considered [17]. For example, in the case of a magnetic dipole oriented in the z -direction, the profile of the B_z component is narrower, having a FWHM approximately equal to d_{SO} [see Fig. 2.11]. Nevertheless, the case of a film edge is of relevance for many applications for instance to 2D magnetic materials [29, 72]. Therefore, in the following discussion I take the effective spatial resolution (considering standoff effects only) to be $r_{\text{eff}} = 2d_{SO}$.

To account for optical effects, Eq. 2.6 in principle needs to be convolved with the optical PSF, assumed to be a Gaussian profile with FWHM d_{opt} . As mentioned, I approximated $d_{\text{opt}} = d_{\text{diff}}$ where d_{diff} corresponds to the diffraction limit, which potentially results in an overestimate of d_{SO} . See below for a detailed attempt to characterise d_{diff} . To account for a finite NV⁻ layer thickness t_{NV} , d_{SO} in Eq. 2.6 is replaced with z , and the average is taken over $d_{SO} \leq z \leq d_{SO} + t_{\text{NV}}$. Thus the magnetic model is:

$$B_{\text{NV}}^* = \frac{1}{t_{\text{NV}}} \int_{d_{SO}}^{d_{SO}+t_{\text{NV}}} dz B_{\text{NV}}(x, z) \circledast \text{Gauss}(d_{\text{opt}}). \quad (2.7)$$

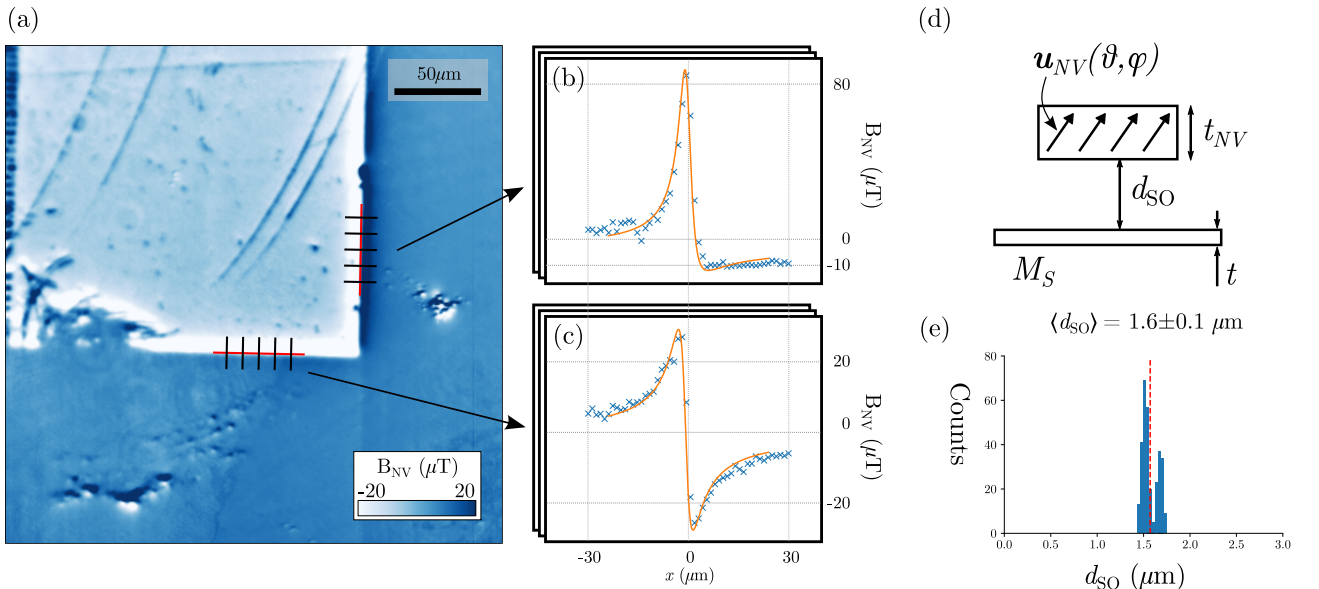


Figure 2.7: (a) Magnetic image centered on a corner of the pad. Note some additional features compared to Fig. 2.4(d), indicating damage to the magnetic film has occurred as a result of repeated cleaning. Line-cuts (black) are taken along segments of edges (red). (b,c) Example line-cuts along perpendicular directions. Orange lines are the magnetic model fit. (d) Diagram indicating model parameters. (e) Histogram of d_{SO} parameter fits to line-cut data. The red line indicates the mean value.

The magnet is assumed to have uniform magnetisation and thickness ($t = 1 \text{ nm}$). Also, the standoff is assumed to be uniform across the image after alignment, hence d_{SO} is uniform. Actually, at alignment, no fringes are visible, hence fringe separation may be taken to be the full image width. This implies the maximum standoff variation between one edge and another is 1 wavelength, i.e. $0.7 \mu\text{m}$. Thus the assumption that standoff is uniform amounts to estimating the average standoff across the image, whereas it would also be possible to map the variable standoff along the edges of the device. Simultaneously fitting pairs of orthogonal line-cuts extracted from two perpendicular edges (edge 1 and edge 2) [Main Fig. 2.7a] recovers the magnetisation M_s , the NV⁻ angles θ and ϕ , and the standoff d_{SO} . Fitting is performed using

Objective	d_{SO}^* (μm)	d_{SO} (μm)	M_s (MAM^{-1})	θ ($^\circ$)
10x	2.20 ± 0.40	1.73 ± 0.41	0.62 ± 0.09	55.30 ± 5.33
20x	2.03 ± 0.09	1.57 ± 0.08	1.03 ± 0.04	52.61 ± 1.70

Table 2.1: Summary of the values obtained for each objective used. d_{SO}^* is the standoff found when the NV^- layer thickness is neglected.

non-linear least squares, with the residual function ϵ of each pair given by:

$$\epsilon = \sum_i [B_{\text{NV}}^*(x_{i,1} - x_1^0, \theta, \phi) + c_1 - y_{i,1}]^2 + \sum_i [B_{\text{NV}}^*\left(x_{i,2} - x_2^0, \theta, \phi + \frac{\pi}{2}\right) + c_2 - y_{i,2}]^2, \quad (2.8)$$

where $x_{i,j}$ and $y_{i,j}$ are the i^{th} coordinate and data point of the j^{th} line-cut respectively ($j \in \{1, 2\}$). The parameters x_j^0 and c_j are to centre the fits to the data horizontally and vertically respectively. A histogram is constructed for each fit parameter. A Gaussian curve is fitted to each histogram, shown in Fig. 2.7 (e) for d_{SO} . This gives the measured value (mean) and an error estimate (\pm one standard deviation), which are the numbers discussed given in Table 2.1. I measured $\theta = 53 \pm 5^\circ$ (10x objective) and $\theta = 48 \pm 5^\circ$ (20x), consistent with the expectation for a $\{100\}$ -oriented diamond (nominally $\theta = 54.7^\circ$). I also measured $M_s = 0.6 \pm 0.1 \text{ MAM}^{-1}$ (10x) and $M_s = 1.03 \pm 0.04 \text{ MAM}^{-1}$ (20x), consistent with the previous measurement of the same sample with scanning NV^- magnetometry [66], $M_s = 0.82 \pm 0.10 \text{ MAM}^{-1}$. Not addressed in this work is the effect of delocalised contributions to the ODMR spectrum of each pixel due to reflections of PL internal to the diamond. In their experiment, Fu et al. estimated this background signal to contribute 50% of measured spectra [13]. Applying the same factor here would result in a doubling of the value of M_s measured. However, systematically determining the ratio of delocalised to local signal was beyond the scope of this experiment, and will be addressed in future work.

2.3.3.2 Optical Resolution

As mentioned, I assumed the optical resolution to be equal to the diffraction limit. However, I did attempt to characterise the optical resolution using the equipment on-hand, as described below. Ultimately this characterisation was inconclusive, hence the approximation made. In future, optical characterisation could be performed using a high resolution microscope target, which is designed to provide a clean image at the sub-micron scale required.

To attempt optical characterisation, NV^- fluorescence (PL) reflectance images were taken of a patterned glass coverslip ($1\mu\text{m}$ gold deposition). Three configurations were imaged: (i) ‘through diamond’, (ii) ‘through glass’ and (iii) directly, as depicted in Fig. 2.8. I found the best resolution was $\sim 1.7 \times$ the diffraction limit, for both the 10x and 20x objective.

I characterised the optical resolution of the system by the full width at half maximum (FWHM) of the point spread function (PSF). The true PSF for an optical system is the Airy disk, which is parametrized by the Airy radius r_0 . However the main lobe of the Airy disk is well approximated by a Gaussian. I imaged gold/glass edges (gold reflects light, glass allows it through, the result is a sharp transition in brightness at the boundary), for which the intensity I along the line-cut is well approximated by the convolution of a Heaviside function and a Gaussian,

$$I \propto 1 + \text{erf} \left(\frac{x}{2\sigma_{\text{optical}}^2} \right), \quad (2.9)$$

where the relation between standard deviation σ_{optical} and FWHM d_{optical} is given by

$$d_{\text{optical}} = 2\sqrt{2 \log 2} \sigma_{\text{optical}}. \quad (2.10)$$

objective	configuration	diffraction limit (FWHM)	d_{optical}	measured limit
		μm	μm	
10	direct	1.1	1.3 ± 0.8	1.2
10	through glass	1.1	4.0 ± 0.9	3.7
10	through diamond	1.1	4.6 ± 1.0	4.3
20	direct	0.7	3.2 ± 0.6	4.5
20	through glass	0.7	2.4 ± 0.4	3.4
20	through diamond	0.7	1.1 ± 7.4	1.5

Table 2.2: Comparison of the diffraction limit and measured optical resolution d_{optical} . The rightmost column gives the ratio of the measured resolution to the diffraction limit - in principle values close to 1 indicate the diffraction limit has been reached.

The optical diffraction limit $d_{\text{diffraction}}$ due to the numerical aperture NA of the objective and wavelength of light λ is

$$d_{\text{diffraction}} = \frac{0.42\lambda}{2\text{NA}}. \quad (2.11)$$

To estimate the actual resolution d_{optical} for comparison with the diffraction limit, I took 300 line-cuts, and built a histogram of the fit parameter from fits with squared residual error $r^2 > 0.9$. I found that distribution of d_{optical} from many line-cuts is well fitted by a skewed Gaussian. The value at the peak is the upper bound on diffraction due to optical distortions. A skewed curve was chosen because although image noise could equally cause over- or under-estimation of d_{optical} , there is a boundary condition that $d_{\text{optical}} \geq 0$. The half width at half maximum (HWHM) of the skewed Gaussian fit is given to indicate the spread, though note that since the distributions are skewed the error is not actually symmetrical.

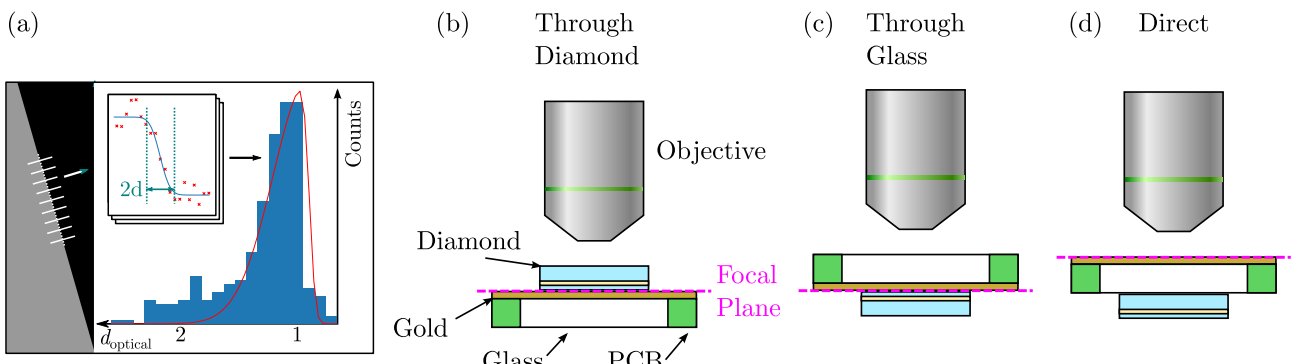


Figure 2.8: (a) Left: schematic of the PL image captured, with line-cuts indicated in white. Right: histogram of the d parameter resulting from line-cut fits (inset). (b-d) Schematics illustrating the configurations tested for optical characterisation.

As can be seen in Table 2.2, although some data is suggestive, such as row 1, overall there are too many competing effects for this method to give a sensitive estimate of the optical resolution. For instance, it appears that in the direct configuration d_{optical} is greater for the higher NA 20x objective than the 10x. This could be because the 20x objective has an adjustable ring, designed to correct for aberration through a cover-slip, however that correction was set to zero according to the ring. It was later found the 20x objective has some optical damage, potentially further confounding these estimates. The 10x objective is also designed to image through a coverslip, hence it is surprising that the estimates through glass/diamond are significantly worse than direct. By the same token, if the 20x aberration correction is indeed zero, it is surprising that in that case the direct measurement of d_{optical} was greater than through

glass. Clearly the 20x through diamond measurement must be disregarded due to the enormous error. Thus these estimates were taken to be inconclusive, although possibly indicative that the diffraction limit is reached. Note that d_{optical} is equal to the diffraction limit only results in a pessimistic overall resolution limit, so better optical characterisation which demonstrated the diffraction limit is not met would improve the overall stand-off estimates made in this work.

2.3.3.3 Optical and Magnetic Resolution

As discussed, resolution can be characterized by three operations: convolution with a Gaussian due to optical effects, convolution with a Lorentzian due to standoff, and averaging over the NV⁻ layer thickness. Note that the Gaussian is an approximation to the diffraction PSF which is an Airy disk, but I used a Gaussian as a more generic optical PSF, allowing us to test the scenario of a PSF broadened by aberrations, $d_{\text{opt}} > d_{\text{diff}}$. However, I found the $d_{\text{opt}} = d_{\text{diff}}$ assumption to give the best fit to the data. To determine the effective resolution mentioned, I found the FWHM of an apparent PSF. This apparent PSF is given by the convolution of the Gaussian and Lorentzian PSFs, neglecting the averaging over the NV⁻ layer for simplicity. The resulting function is the Voigt profile. To account for the NV⁻ layer thickness, the Lorentzian PSF FWHM $2d_{\text{SO}}$ is replaced with FWHM $2d_{\text{SO}}^*$, where d_{SO}^* is the apparent standoff determined by fitting the line-cuts to the data without including the averaging of the NV⁻ layer [See Table 2.1]. As expected, I found $d_{\text{SO}}^* \approx d_{\text{SO}} + t_{\text{NV}}/2$. The FWHM of a Voigt profile r_V composed of a Gaussian of FWHM r_G and Lorentzian of FWHM r_L is well approximated by [73]

$$r_V = 0.5346r_L + \sqrt{0.2166r_L^2 + r_G^2}. \quad (2.12)$$

Thus the effective resolution r_{eff} is given by

$$r_{\text{eff}} = 0.5346 \times 2d_{\text{SO}}^* + \sqrt{0.2166 \times (2d_{\text{SO}}^*)^2 + r_{\text{opt}}^2}. \quad (2.13)$$

To illustrate the next steps in improving resolution, I graphed NV-sample standoff against effective resolution for objectives with different numerical apertures [Fig. 2.9]. The measurements made in this work using the 10x and 20x objectives are shown. At zero standoff, the effective resolution is equal to the diffraction limited resolution.

2.3.4 Optical Profilometry

As discussed, an obvious requirement for standoff minimisation is that the sample and diamond surfaces are flat and free of protrusions. I characterised both the diamond and sample using optical profilometry. Note that (without further analysis) profilometry assumes the same material across the image, whereas for the sample there are different materials present, such as the large damaged region where the silicon substrate is exposed. Nevertheless, the protrusions from both surfaces appear to be sufficiently small: $\leq 0.5 \mu\text{m}$. Compared with the standoff distances measured, this indicates polishing and cleanliness were not limiting. This detail will require further attention in order to reach the diffraction limit, which requires $\sim 100 \text{ nm}$ standoff.

2.3.5 Results and outlook

The analysis of Fig. 2.7(a), which was obtained using the 20x objective, leads to $d_{\text{SO}} = 1.6 \pm 0.1 \mu\text{m}$ [Fig. 2.7(e)]. Similarly, from the image in Fig. 2.4(d) which used the 10x objective, I found $d_{\text{SO}} = 1.7 \pm 0.4 \mu\text{m}$. Such physical standoffs are similar to the best values reported by dropping the diamond and manual trial and error [58, 74], and significantly improved compared to more typical values on the order of $10 \mu\text{m}$ [13, 28, 34, 75]. Together, the standoff and optical resolution combine to give an effective spatial resolution for a magnetic edge of $\approx 4 \mu\text{m}$. This value is dominated by the effect of standoff, as the stray field over an edge has a width of $2 \times d_{\text{SO}}$ [76]. Including NV⁻ layer thickness, the contribution due to standoff is roughly $4 \times$ that of diffraction, hence improvements to the effective resolution should first

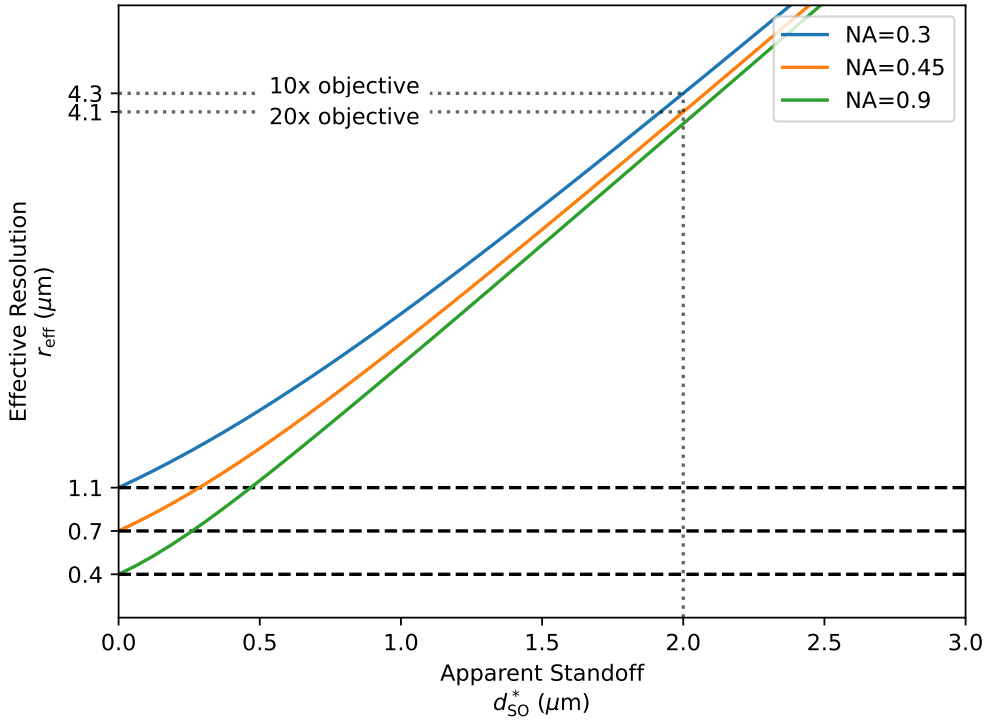


Figure 2.9: Effective resolution vs apparent standoff (or actual standoff, neglecting NV^- layer thickness). Black dashed horizontal lines indicate diffraction limited resolution. Grey dotted lines roughly correspond to the situation for the measurements in Table 2.1.

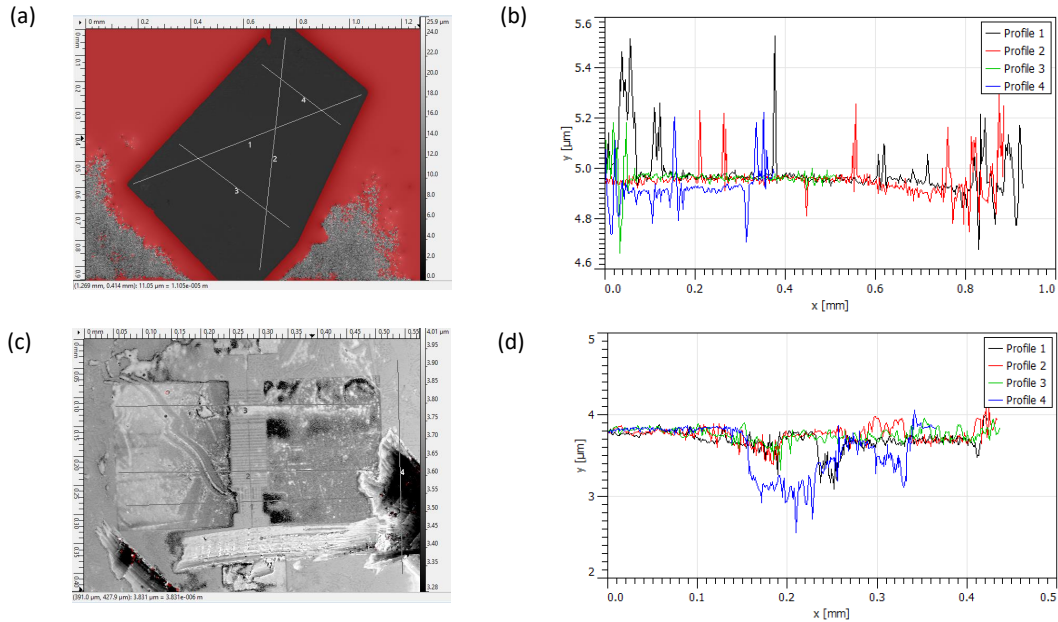


Figure 2.10: (a) Topographic image of the diamond used in the widefield probe. (b) line-cuts of the diamond surface, indicating only protrusions less than $0.5 \mu\text{m}$ (c) Topographic image of the magnetic device. (d) line-cuts of the device surface, indicating only protrusions less than $0.3 \mu\text{m}$ above the surface.

involve further minimization of d_{SO} , followed by improvements to r_{opt} and finally the diffraction limit. For a magnetic dipole, the stray field width is approximately equal to d_{SO} , giving a resolution of $\approx 2 \mu\text{m}$

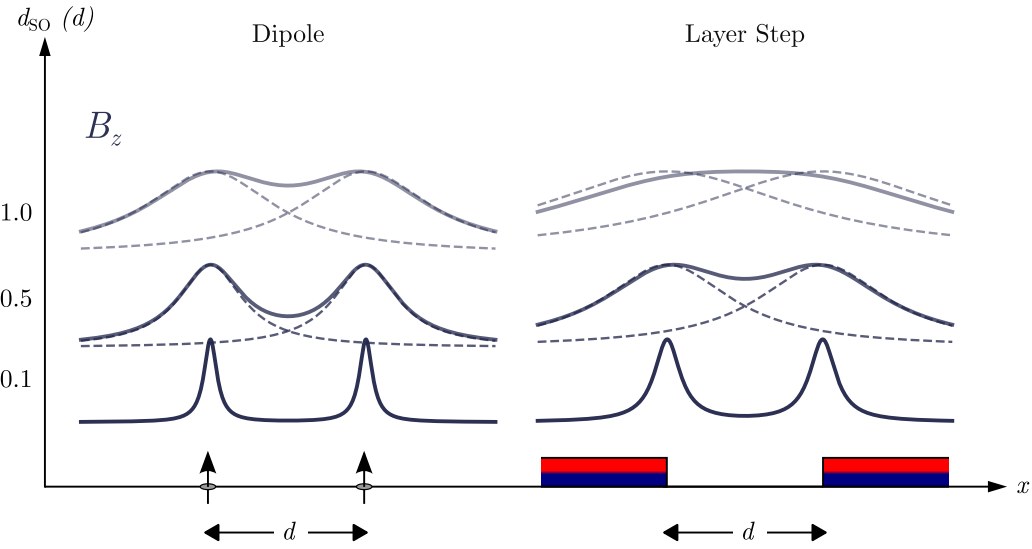


Figure 2.11: Illustration of the z -component of the stray magnetic field B_z due to two magnetic dipoles (left) and two magnetic edges (right) at separation d , with the NV^- sensing layer at various standoffs d_{SO} from the magnetic sources. For the dipoles, the resolution is d , beyond which they cannot be resolved to two separate points. For the edges, they can be resolved up until $d_{\text{SO}} = 0.5d$, or equivalently $d = 2d_{\text{SO}}$.

in this case when trying to resolve dipole-like magnetic objects.

Overcoming standoff limitations will require finer angular and vertical control of the probe, easily accomplished using robotic stages [60]. Keeping the surfaces clean and flat to further reduce d_{SO} should be readily achievable. Neglecting NV^- layer thickness, to attain an effective resolution roughly $1.2\times$ the diffraction limit for a $\text{NA} = 0.45$ objective requires the standoff d_{SO} to be $\sim 150 \text{ nm}$. Dust particles in air are typically $1 - 100 \mu\text{m}$ in size, thus a clean-room environment may be required to prevent contamination. To ensure the NV^- layer thickness is not limiting, diamonds with a thinner ($\lesssim 100 \text{ nm}$) layer should be used, at the expense of a reduced magnetic sensitivity [63]. Secondly, diffraction-limited optical resolution should be attainable by using a thinner diamond or customised optical components to minimise aberrations. A final resolution improvement can be achieved by lowering the diffraction limit, down to 350 nm using an objective with $\text{NA} = 0.9$. This will require some optimisation of the widefield probe design to accommodate the millimetre-scale working distance of such high-NA objectives.

2.3.6 Future directions

In 2021, our group published a review of widefield NV microscopy [5]. I authored the ‘Ease of use’ section, which is adapted here in order to illustrate our vision of a next generation NV^- widefield microscope. I presented a few directions for future work to overcome current challenges pertaining to usability in operation and flexibility of application. The proposed technological developments are illustrated in Fig. 2.12.

2.3.6.1 Automation

In addition to interfacing, many tasks pertaining to the operation of the NV^- microscope can in principle be automated: auto-focusing the optics, aligning the bias field vector (e.g. via control of a Helmholtz coil system) to split the NV^- families, rotation of a half-wave plate in the excitation path to maximise ODMR contrast, and setting the microwave and pulsing parameters to optimise magnetic sensitivity. Additionally, measurement and processing of the ODMR signal, such as determining which microwave frequencies to scan and where the peaks are located could be tackled, for example, using Bayesian design. [62]

Such an automated setup would greatly improve the ease of use of the widefield NV^- microscope, and enable rapid sample exchange for high throughput measurements.

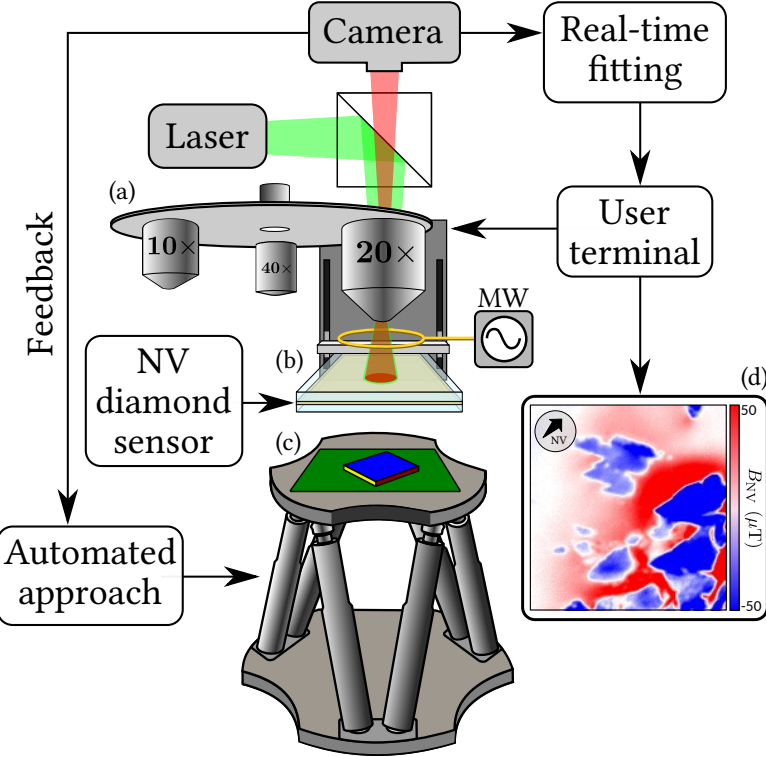


Figure 2.12: Illustration of a widefield NV⁻ microscope implementing features to support streamlined user operation. Objectives of various magnification are mounted to a turret (a) for rapid interchange. The diamond sensor (b) is mounted separately to the sample (c), so that different samples can be imaged without affecting the sensor configuration. The sample (c) sits on a stage with orientation control (e.g. a hexapod). Together with feedback from the camera, this enables “automated approach”: automatically bringing the sample and sensor surfaces into alignment and contact. Once sensor-sample alignment is completed, the user can view the magnetic image in real-time (d) e.g. using GPU accelerated data processing. Components not to scale.

2.3.6.2 Interchangeable optics

For measurements where the resolution can be diffraction limited (rather than by NV-sample standoff or NV⁻ layer thickness) it may be desirable to use a low magnification, high field of view objective for initial alignment and holistic characterisation or to find the area of interest, before switching to a high magnification and high numerical aperture objective for high resolution imaging. Therefore, easily interchangeable optics, e.g. through a selection of objective lenses mounted on a turret [Fig. 2.12(a)], would be a desirable feature.

In this case, epifluorescence illumination is advantageous as the laser spot size will scale with the imaging field of view. Furthermore, the magnetic sensitivity per camera pixel is conveniently preserved upon changing objective, up to a correction factor to account for the change in collection efficiency, spin repumping efficiency and related effects. This conservation property is due to shot-noise sensitivity's equal and inverse scaling with image magnification and laser spot size diameter [41]. One drawback of the epifluorescence geometry is that the sample is directly illuminated by the laser, which can cause significant heating. Alternatively, side illumination via a light sheet [77] or total internal reflection [36] may be employed, at the drawback of requiring another set of interchangeable optics to adjust the laser spot size.

2.3.6.3 Rapid data processing

In a typical experiment performed today, there can be a large time delay between signal acquisition and magnetic image data being available for sample analysis. In principle, the only physical limiting factor is the integration time, however in practice data transfer and processing also introduces a significant

delay. In a widefield ODMR experiment, acquisition can easily reach data rates of order gigabits per second (Gbps). For example, a standard 4 megapixel camera with 30 ms exposure time and 16-bit depth produces data at 2 Gbps. While USB3 can handle this, processing such quantities of data as it arrives is nontrivial. For this reason, experiments generally proceed without continuous in-acquisition data processing. The ODMR data is then fitted upon request by the user to quantitatively map parameters of interest, such as magnetic field. This processing may take up to several minutes, or even hours.

However, modern data fitting techniques can dramatically speed up this processing time, for example via utilisation of a Graphics Processing Unit (GPU) which can take advantage of the embarrassingly parallel problem of performing pixel-wise peak fitting. [78] Integrating and optimising the data acquisition, processing and storage pipeline is feasible with present day technologies, and could enable the magnetic field map to be displayed and refreshed on a time scale of order seconds (i.e. after every single ODMR frequency sweep) [Fig. 2.12(d)]. Such rapid feedback would result in a user experience more akin to that of an optical microscope making NV⁻ microscopy more attractive for high throughput measurements.

2.3.7 Conclusion

In summary, this chapter demonstrated an NV⁻ microscope based on an integrated widefield NV⁻ probe which provides a rapid and reliable way to interface the probe with the sample, making this system ideal for high-throughput measurements of a range of magnetic samples and electronic devices. From the analysis of spatial resolution, I found the effective spatial resolution to be dominated by standoff. With further optimisation of the spatial resolution and automation of the alignment procedure, there is an excellent prospect for this instrument to become a routine magnetic imaging technique.

Chapter 3

Demonstration of Widefield Imaging of Spin Defects in Hexagonal Boron Nitride

This work was the result of a collaboration between our group and the Aharonovich group (University of Technology Sydney) established in June 2021. It is a preliminary study into the boron vacancy (V_B^-) in hexagonal boron nitride (hBN), an exciting and recent contender material for quantum sensing. We received a sample in July, which I imaged throughout July - August. Initial results were poor, because we did not have an appropriate high pass filter (the sample has a strong background fluorescence, and the V_B^- defect fluoresces quite weakly). In August we acquired a 750 nm high pass filter, with which ODMR was then clear and consistently achievable. Between August and October I took the widefield ODMR measurements, and processed spin-dynamic measurements. The latter lab measurements were taken by Dr. J.-P. Tetienne, as I was writing this thesis.

3.1 Introduction

Hexagonal boron nitride (hBN) is a van der Waals (vdW) material¹ consisting of one or more 2D layers of hexagonal B-N lattices [Fig. 3.1 (a)]. The bulk crystal can be exfoliated down to a chemically stable mono-layer. Since 2010, hBN has found excellent application as an encapsulate of other 2D materials, in particular graphene, for insulation and passivation. More recent discoveries reveal hBN to be, in and of itself, a material with interesting electronic and optical properties [79]. Of particular interest here is its ability to host stable quantum defects (much like the NV⁻ in diamond), which may enable its use as a quantum sensor of temperature, pressure, and magnetic field via ODMR imaging. In Chapter 1 a key limitation to quantum diamond microscopy discussed was the NV-sample standoff distance, which is difficult to overcome while retaining practicality. In Chapter 2 we proposed a novel application of orientation alignment to address this issue, however the resolution is still fundamentally limited by the NV-layer thickness and implantation depth. In this chapter, an exciting new approach using hBN instead of NV⁻ is explored. It is possible that with three layers of hBN (the middle hosting defects) a stable, ultra-thin quantum sensor can be realised, with a fundamental standoff limit of a single atomic layer.

Since 2016, a large number of optically active defects have been discovered in hBN. A brief summary of those developments are given here, which illustrates the rapid pace at which this field is progressing. Room temperature quantum defects in hBN were first identified in 2016 by Tran et al. [80]. These were verified as single photon emitters by means of Hanbury Brown and Twiss interferometry. As of 2019, a number of defects showing magnetic-field dependent transitions had been identified [81, 82], but ODMR had yet to be established [79]. In May 2020 Gottscholl et al. [20] reported ODMR of an hBN colour centre at room temperature, and identified it as the negatively charged boron defect (V_B^-), created via neutron irradiation. It is due to this defect that hBN is now seen as a possible contender for quantum sensing applications.

The V_B^- colour centre is a point defect with D_{3h} symmetry, where a single B atom is removed from its lattice site. It can be engineered by means of neutron or charged ion (e.g. H^+) irradiation, both well established techniques. The defect forms an atom-like spin triplet ($S=1$) system with a ground state that exhibits zero field splitting (ZFS) at frequencies $f_{1,2} = (D \pm E)/h$, where h is Planck's constant, D and E are temperature, strain and pressure dependent parameters. The ZFS is thought to be induced by dipolar interactions between unpaired electrons, resulting in the triplet degeneracy being lifted. When a magnetic field \mathbf{B} is applied along the c hexagonal crystal axis (out of plane), that axis is the quantisation

¹In-plane bonding is covalent, but interlayer bonding arises from weak vdW forces.

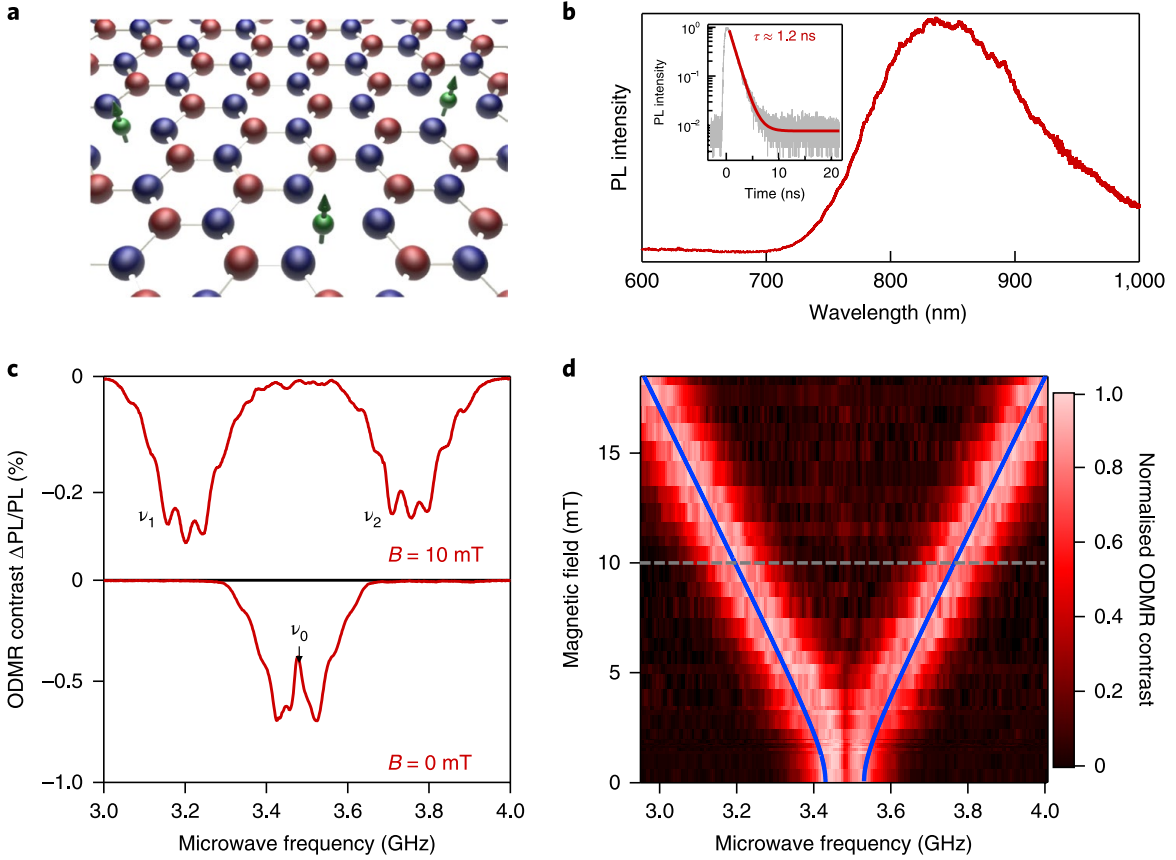


Figure 3.1: (a) Hexagonal boron (red) nitride (blue) lattice with boron vacancy spin defects (green). (b) Photoluminescence (PL) spectrum of an hBN sample following H^+ irradiation. Inset: fluorescence lifetime measurement yielding $\tau = 1.2$ ns. (c) ODMR spectrum of the V_B^- in hBN under zero bias field and 10 mT. (d) Waterfall ODMR spectrum showing the linear relationship between magnetic field and spin resonance frequency. Reproduced with permission from Ref. [20].

axis (defined to be the z -axis), and the system can be driven to the spin $m_s = \pm 1$ projections under application of resonant microwave frequencies at

$$f_{1,2} = (D \pm \Delta)/\hbar, \quad (3.1)$$

where $\Delta/\hbar = \sqrt{(E/\hbar)^2 + (\gamma B)^2}$ is the splitting parameter, $\gamma = g\mu_B$ is the gyromagnetic ratio, g is the Landé factor and μ_B is the Bohr magneton. The Landé factor for V_B^- has been found to be almost isotropic, with $g = 2.000$ [20]. Optical pumping at 532 nm results in excitation from the ground state to an excited state. The excited state lifetime is 1.2ns (c.f. 10ns for NV⁻ in diamond), and the subsequent emission has a maximum intensity at 850nm [Fig. 3.1 (b)]. From the excited state, an ISC to a meta-stable state occurs selectively to spin polarised states. The decay path via the meta-stable state is non radiative, thus fluorescence is decreased when a resonant microwave field is applied [Fig. 3.1 (c) and (d)]. Like the NV, the existence of the ISC enables spin polarisation of the system with optical pumping.

3.2 Properties of the V_B^- in hBN

As with the NV⁻ in diamond, it is important to understand the photo-dynamics of the V_B^- in order to optimise ODMR and other sensing protocols. There is still much work to be done determining the energy structure of the V_B^- , however some details are known. ODMR measurements performed by Gottscholl et al. [20] and seen in Fig. 3.1 (d) yield $D/\hbar = 3.48$ GHz and $E/\hbar = 50$ MHz at $T = 300$ K. The gradient of the fit in Fig. 3.1 (d) yields the result $g = 2.000$. Given the similarity in ODMR response to the NV⁻ ODMR, a phenomenological energy diagram and Hamiltonian can be constructed analogously, as described above. The inset to Fig. 3.1 (b) indicates a fluorescence lifetime of $\tau_{exc.} \approx 1.2$ ns.

Ab-initio simulation provides further insight. The theoretical energy diagram for the V_B^- calculated by Reimers et al. [83] at room temperature (295 K) is shown in 3.2. This structure is significantly more complex than the NV^- picture (in part because the NV^- discussion was simplified), however we see that, as with the NV, the system can be excited (vertical absorption) into high energy states, from which it will quickly relax to excited states, and then decay radiatively or non-radiatively (spin dependence is not explicitly shown here). The main direct PL transition (thick purple) has a rate of $1/11 \mu\text{s}$ whereas the ISC transition out of the excited 3A_2 state has a rate of $1/1.7 \text{ ns}$, which together are consistent with the experimental result that $\tau_{\text{exc.}} \approx 1.2 \text{ ns}$. However, we also see that the ISC return path is extremely slow, with a rate of 1.8 s . This suggests a weak signal response, as the re-pumping rate is limited to seconds (compared with NV, which we recall has an ISC return rate of 200 ns). Critically, the ISC path has probability 99.98%, meaning the quantum efficiency is only $\sim 0.02\%$, implying decay is primarily non-radiative. Therefore, the fluorescence will be very weak, motivating a laser excitation power near saturation.

Turning now to the spin-dynamics, we consider the parameters T_1 , T_2 and T_2^* . As introduced in Chapter 1, the spin-relaxation time T_1 describes the transition rate from spin polarised (e.g. $|0\rangle_g$) to the thermal mixed state. The dephasing time T_2^* describes the rate at which the ensemble loses phase coherence due to magnetic noise. Additionally, we also consider the decoherence time T_2 , which is essentially the dephasing time were the spins in a homogeneous magnetic environment (see below for details).

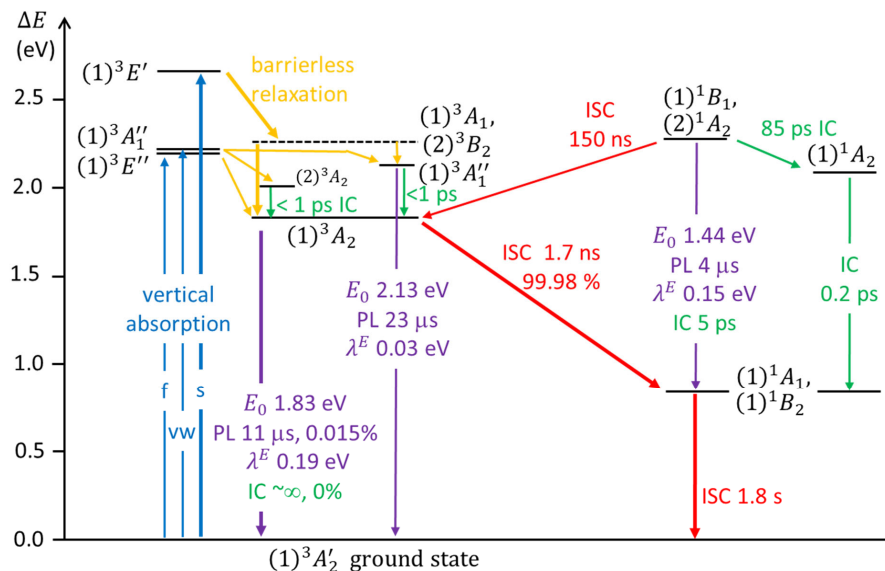


Figure 3.2: Theoretically calculated energy level diagram for the V_B^- in hBN at room temperature. The represented processes are: blue: photon absorption; orange: barrierless ultrafast relaxation to zero phonon lines; green: internal conversion (IC); red: intersystem crossing (ISC) purple: photoluminescence (PL). The thicker lines indicate the critically perceived processes during the photocycle, which are the most relevant to the discussion given here. Singlet and triplet states are labelled by their associated irreducible representations. Further details, including uncertainties are discussed in [83]. Reproduced from [83] with permission.

3.3 Methods

3.3.1 hBN Sample

The hBN sample used here was engineered by the Aharonovich group at the University of Technology Sydney, similar to the samples in [84]. From a bulk crystal, hBN flakes were transferred onto a silicon substrate and subsequently homogeneously irradiated with a hydrogen ion beam at equivalent energy 15keV/ H^+ ion. The flakes are $\sim 290 \text{ nm}$ thick, and the simulated peak implantation depth is $\sim 175 \text{ nm}$.

3.3.2 Setup

I used the widefield system described in Chapter 2 for initial measurements, before moving to the system described in Chapter 4 (with all NIR components removed). The V_B^- fluorescence spectrum is peaked at ~ 850 nm [Fig. 3.1 (b)], but we also measured significant fluorescence between $600 - 700$ nm (of unknown source), initially swamping the V_B^- signal. With the introduction of a 750 nm long pass filter this was overcome, and we were able to perform ODMR (below) with as much as $\sim 5\%$ contrast for defects in the centre of the illumination beam. Due to its low quantum efficiency and long dark-state lifetime, laser intensity needed to be as high as possible to ensure a measurable photo-response. In both setups, the beam-expander was removed, and a $20\times$ objective (NA 0.45) used to focus the ~ 300 mW beam to a $\sim 200 \mu\text{m}$ diameter spot. The laser is gated by an acoustic-optic modulator (AOM), which importantly has a ~ 100 ns rise (and fall) time. We found that shorter initialisation/readout pulses gave better contrast, hence 200 ns laser pulses were used such that peak laser power is reached 100 ns into the pulse.

The V_B^- has ZFS at 3.5 GHz (c.f. the NV at 2.87 GHz), which none of the microwave generators in the lab can operate at, apart from the Windfreak NV⁻ used in Chapter 2. Thus when moving to the Chapter 4 system, I replaced the existing RF setup with the setup described in Chapter 2, which involved some re-wiring and LabVIEW modifications. The amplifier on this setup has a range up to 4.3 GHz, which limited the strength of the bias field which could be applied – in Fig. 3.6 (j) the ODMR resonances are maximally split given the amplifier limit. The amplifier maximum power output is ~ 20 W, which we found was saturated with an input power of 6 dBm (despite the Windfreak NV⁻ having a nominal maximum output power of 18 dBm). Due to the weak photo-response, achieving sufficiently high contrast ODMR for mapping required as high microwave power as possible. Initially, contrast was limited for most flakes to $\sim 2\%$, when driving at maximum microwave power. To improve this, I fabricated a new microwave antenna using much thinner copper wire, thereby increasing the current density and (by Biot-Savart) radiated field strength. This led to an $\sim 2\times$ improvement in contrast. Note that while increasing microwave power, we did not notice increased line-width broadening, suggesting the microwave power is not causing significant power broadening. This was also verified using an NV⁻ embedded diamond [Fig. 3.3 (c)] as a calibration: from [20] the FWHM for a single resonance is expected to be ~ 50 MHz (similar to the hyperfine splitting constant). At full microwave power, the NV⁻ ODMR line-width was only ~ 10 MHz. Given the NV⁻ environment response is on the order of megahertz, the ODMR line-width is effectively due to the instrument response. Power broadening will occur when the instrument response width is larger than the environment response width, but at current levels we are not in that regime. In future, it is desirable to further increase the microwave power delivery (up to the point that the response widths are approximately equal), which will improve the contrast between the hyperfine peaks.

3.3.3 Pulsed Protocols

In Chapter 1, we introduced the ODMR protocol, used to probe the spin state of a quantum defect, and thus perform magnetic, strain, and temperature sensing. Here, we introduce three more protocols, designed to investigate the dynamics of the defect, namely the Rabi frequency Ω_R , T_1 , T_2 and T_2^* .

3.3.3.1 Rabi

The Rabi protocol is used to determine the Rabi frequency Ω_R associated with driving a two-level spin system with a time-varying magnetic field (the microwave field). To determine Ω_R given a static background field and microwave power, the Rabi sequence is to first spin polarise the ensemble to $|0\rangle_g$, then microwave drive the system for a time τ , then readout the ensemble state. Repeating this over a range of values of τ we thus measure the Rabi cycles, and hence determine Ω_R . However, due to the finite dephasing time T_2^* , as the length of the microwave pulse increases so does the amount of dephasing due to each defect having a unique local magnetic environment. Thus the PL signal is damped by a decay

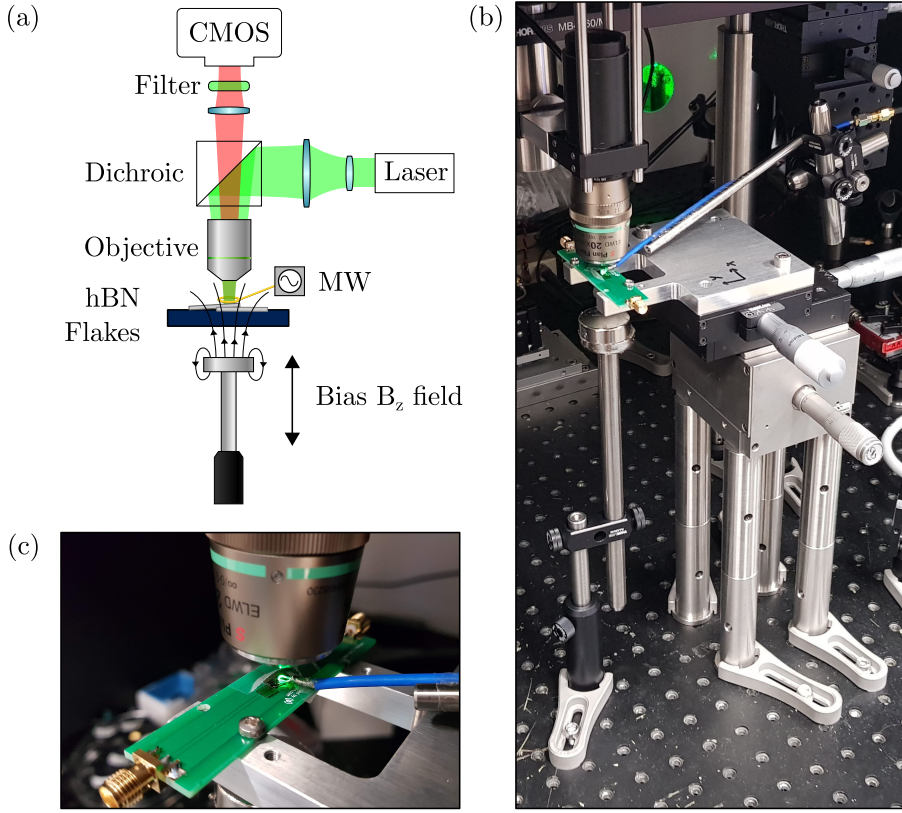


Figure 3.3: (a) Schematic of the setup, with adjustable B_z field. For zero field experiments, the magnet is removed altogether. (b) Image of the setup. (c) Closeup image of the hBN sample on silicon, on a printed circuit board. Next to the sample is an NV^- embedded diamond, used for initial calibration of the microwave power as described in the text.

to thermal mixture, and hence the response \mathcal{I} is a modulated Rabi cycle

$$\mathcal{I}(\tau) = Ae^{-\tau/T_2^*} \cos(2\pi\Omega_R\tau) + \mathcal{I}_0, \quad (3.2)$$

where A and \mathcal{I}_0 are properties of contrast and collection efficiency.

3.3.3.2 Spin Relaxation

As mentioned, spin relaxation is the process by which a polarised ensemble returns to a thermally mixed state. The rate is simply measured by first polarising the system, then waiting a time τ before readout. Scanning τ and recording the PL for each value results in an exponential decay curve, with decay constant T_1 .

3.3.3.3 Spin Echo

Once the Rabi frequency is ascertained, advanced pulse sequences which rely on precision timing to drive the spin polarisation can be employed. For example, consider a system initially polarised in the $|0\rangle_g$ state. A microwave pulse applied for time $1/2\Omega_R$ will drive the system to the $|\pm 1\rangle_g$ state. By convention, instead of referring to pulse durations in terms of the Rabi frequency (which is dependent on factors such as microwave power and background magnetic field), we introduce the Bloch sphere terminology as follows. The two-level system has two orthogonal states labelled $|0\rangle$ and $|1\rangle$. The system state is given by $|\psi\rangle$. Without loss of generality, we can write the state as a Bloch vector,

$$|\psi\rangle = \cos(\theta/2)|0\rangle + e^{i\phi}\sin(\theta/2)|1\rangle, \quad (3.3)$$

where $\theta, \phi \in [0, 2\pi]$ (ϕ is the ‘phase’ referred to in the dephasing rate T_2^*). The $1/2\Omega_R$ duration pulse results in $\theta = 0 \rightarrow \theta = \pi$, hence it is referred to as a π -pulse. Similarly, a $\frac{\pi}{2}$ -pulse would drive the $|0\rangle_g$

system to a perfect superposition of $|0\rangle_g$ and $|+1\rangle_g$ (or $| -1 \rangle_g$, depending on the orientation of the field and defect).

Referring to the diagram in Fig. 3.4 (e), first, the system is initially polarised. Then, a $\frac{\pi}{2}$ -pulse drives the system to a mixed state. Next, the system undergoes free procession for a time $\tau/2$. The blue and purple Bloch-vectors are defects with a different local magnetic environment compared to the black Bloch-vector, hence different Larmor frequencies resulting in a spread over time. The pulse sequence removes this effect with a π -pulse, after which the ‘fast’ (blue) defect spins catch-up to the ‘slow’ (purple) defect spins during another equal free procession time $\tau/2$. Finally a $\frac{\pi}{2}$ -pulse is applied and readout performed. Because the high frequency dephasing due to in-homogeneous local magnetic environments has been removed, the measured exponential decay rate is T_2 rather than T_2^* .

3.4 Preliminary results

3.4.1 Measurement of Spin Dynamics

Dynamic measurements were performed by J.-P. Tetienne and myself using the setup and pulse sequences described above. In practice, the pulse protocols are modified to include a reference sequence (as with CW ODMR). In our setup, a camera is used to image the defect PL signal. For each value of τ , the sequence is repeated N times to improve signal to noise ratio. The camera exposure lasts the full N iterations, thus a time $N(\tau + c)$ where c is a constant. As τ increases, the camera exposure increases, hence it is critical that the signal is normalised as the PL signal measured will increase simply due to increasing exposure time. In the case of Rabi, the reference sequence is identical to the signal sequence, except no microwave is applied. In the case of T_1 and spin echo, an extra π -pulse is added before readout, inverting the PL. In all cases, the final measured signal is the contrast, defined as

$$\text{ODMR Contrast} = \frac{\text{signal} - \text{reference}}{\text{reference}}. \quad (3.4)$$

Here we compare our results (all at zero bias magnetic field) with those of Gottscholl et al. [48]. From Fig. 3.4 (a), we see that $T_2^* \approx 140$ ns, which is comparable to the reported 100 ns. However, we measured a T_1 time of ≈ 4.2 μ s [Fig. 3.4 (b)], significantly shorter than the reported 18 μ s, meaning the defects in this hBN flake are (for as yet undetermined reasons) possibly less stable than those reported (T_1 relaxometry provides an upper bound for T_1 , as there may be other non-thermal influences, though notably magnetic field is likely not one of them [48]). Finally, from Fig. 3.4 (c) we estimate $T_2 \approx 2$ μ s, which is consistent with the reported measurement of $T_2 \approx 2$ μ s at bias field $B_0 = 8.5$ mT and $T_2 \approx 3$ μ s at $B_0 = 15$ mT. Overall, our results are broadly consistent with those reported.

3.4.2 Performing Widefield Quantum Imaging with hBN

I performed widefield ODMR imaging at room temperature, using the setup described above. In Fig. 3.5 (a), we see the optical (PL) image of a flake. The bright lines in the middle of the flake appear to be cracks. In general, I found that cracks in flakes had a higher PL response. This may be due to a higher defect concentration at the edges, or an optical scattering effect at the boundaries. In this experiment, a bias field of ~ 90 G was applied, hence the splitting seen in the averaged ODMR response in Fig. 3.5 (b). We see that fitting a sum of two Lorentzians (red) recovers the peaks, but is not a particularly good fit to the lineshape. This is because the model fitted here does not include hyperfine peaks, which are visible (see Fig. 2 (d) of [20] for comparison), and indicated with grey dashed lines. Nevertheless, in this initial investigation, for the purpose of mapping magnetic fields, fitting the sum of two Lorentzian functions is sufficient.

Fitting to each pixel ODMR rather than the average, we construct a 2D map of the ZFS D parameter [Fig. 3.5 (c)], and the strain and z -magnetic field Δ/h [Fig. 3.5 (d)]. Considering first the D map, we see the average shift is ~ 3454 MHz, which corresponds to room temperature (see Fig. 2 (c) of [24]). The

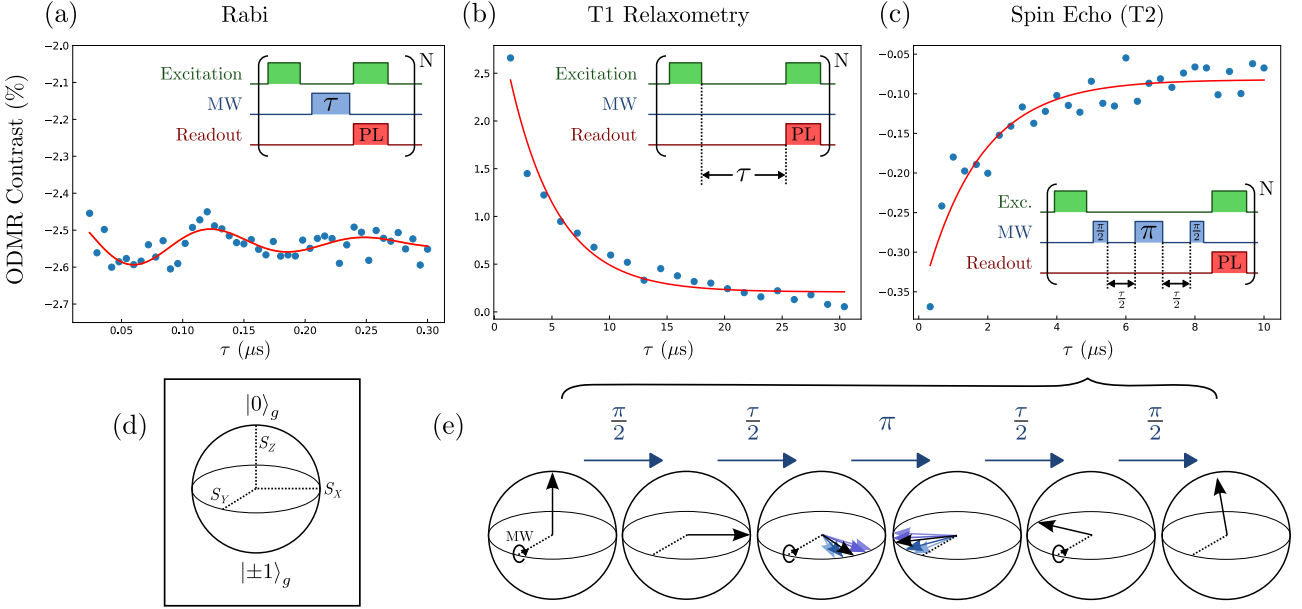


Figure 3.4: Data collected from the flake shown in Fig. 3.6 (a). ODMR contrast calculated according to Eq. 3.4. (a) Rabi sequence, where the length of the microwave pulse is scanned to determine the π -time. Fitting Eq. 3.2 yields a π -time $\approx 60 \text{ ns}$ and $T_2^* \approx 140 \text{ ns}$. (b) T_1 relaxometry, where τ is scanned to determine the rate of relaxation from $|0\rangle_g$ to the thermal mixed state. The exponential fit shown yields $T_1 \approx 4.2 \mu\text{s}$. (c) Spin echo (a.k.a. Hahn echo) sequence, where τ is scanned to determine the decoherence time T_2 . The exponential fit shown yields $T_2 \approx 2 \mu\text{s}$. Given the pulse sequence and reference described in the text, one would expect the PL signal to decrease with increasing τ . However, as can be seen in the Rabi plot, due to the short T_2^* time, a $3\pi/2$ -pulse ($\tau = 90 \text{ ns}$) results in significant dephasing during the pulse, which here resulted in inversion of the signal and reference. (d) Bloch sphere for the spin defect ground state. Note this is really two Bloch spheres overlaid - one for the two level system $a|0\rangle_g + b|+1\rangle_g$ and one for the two level system $a|0\rangle_g + b|-1\rangle_g$. (e) Bloch sphere representation of the spin echo sequence of (c). ‘Fast’ phase decoherence (which results in T_2^*) is recovered by the π -pulse, demonstrating why spin echo is T_2 limited rather than T_2^* .

temperature variation due to a $\sim 10 \text{ MHz}$ shift would be $\sim 6.2 \text{ K}$ [24], but could also be influenced by pressure and axial strain. The image in Fig. 3.5 (d) has a shift correlated with the crack in the fluorescence image. Because $\gamma B_z \gg E/h$, we have $\Delta/h \approx \gamma B_z$, however it is unlikely that the $\sim 2 \text{ G}$ variation is due to intrinsic magnetisation of the flake. This feature may be due to the crack impacting the local defect lattice environment in a way not captured by Hamiltonian in Eq. 1.1.

To explore this further, I briefly investigated strain, and the effect of changing the bias magnetic field, using another more complex flake shown in Fig. 3.6 (a). In Fig. 3.6 (e), zero bias field is applied ($B_z = 0$) hence a strain map of off-axial parameter E is produced ($E/h \gg \gamma B_z \implies \Delta \approx E$). We see a variation in E/h of about 5 MHz, with a mean value of $E/h \approx 50 \text{ MHz}$, which is consistent with the flake not under pressure and on a flat surface, though the details of the E dependence on strain are yet to be determined. It has been established that E is largely temperature independent [24].

Increasing the bias field to $\sim 80 \text{ G}$ in Figs. 3.6 (c) and (f), in (c) we see an overall increase in D . Increasing the bias field further to $\sim 200 \text{ G}$ in Figs. 3.6 (d) and (g), there is another increase in D . This is consistent with an off axis bias field. To estimate the deviation angle θ of the bias field from the z -axis, I wrote a script to calculate the eigenenergies of Eq. 1.1 under an arbitrary bias field. The “intrinsic” value of D (D_0) was estimated from Fig. 3.6 (b) (zero bias field). Using Least-Squares optimisation to fit the simulation outputs (D and Δ) simultaneously to the results at 80 G and 200 G bias field, I estimated $\theta \approx 19^\circ$.

In Figs. 3.6 (e-g), there appears to be large magnetisation occurring, with variations of roughly 5 MHz, 10 MHz and 15 MHz across the flakes respectively. Again, it is unlikely that such variation is due to mag-

netisation (although perhaps the flake is contaminated). Similarly, the variations in D/h in Figs. 3.6 (b-d) are roughly 10 MHz, 5 MHz and 10 MHz respectively. One possibility is that due to the off-axis bias magnetisation, there is mixing between strain induced D shifts and Δ . I briefly explored this by again using Eq. 1.1, but found $\delta E/\delta D \ll 1$ (variations in E caused insignificant variations in D , and vice-versa). These results held with the bias field at 80 G and 200 G, and spherical orientation (θ, ϕ) at $\theta = 19^\circ$, for various angles of ϕ . This suggests that the patterns observed are due to more complex strain phenomena, which will require further investigation. The Hamiltonian in Eq. 1.1 is a simplified model, which has proved useful for studies utilising the NV in diamond where strain can be mostly neglected (such as in Chapter 2). However, stress tensor imaging with the NV requires a more complete (though still simplified) Hamiltonian [85], and theoretical characterisation of the NV reveals a complex picture of strain interaction [86]. The results here suggest a similarly detailed characterisation of strain in hBN will be required to understand its response. Other effects may also be present. For example, the stacking of the vdW layers could result in different local V_B^- environments, resulting in the ensemble response being the combination of different “families” (by analogy with the 4 crystal axes of the NV).

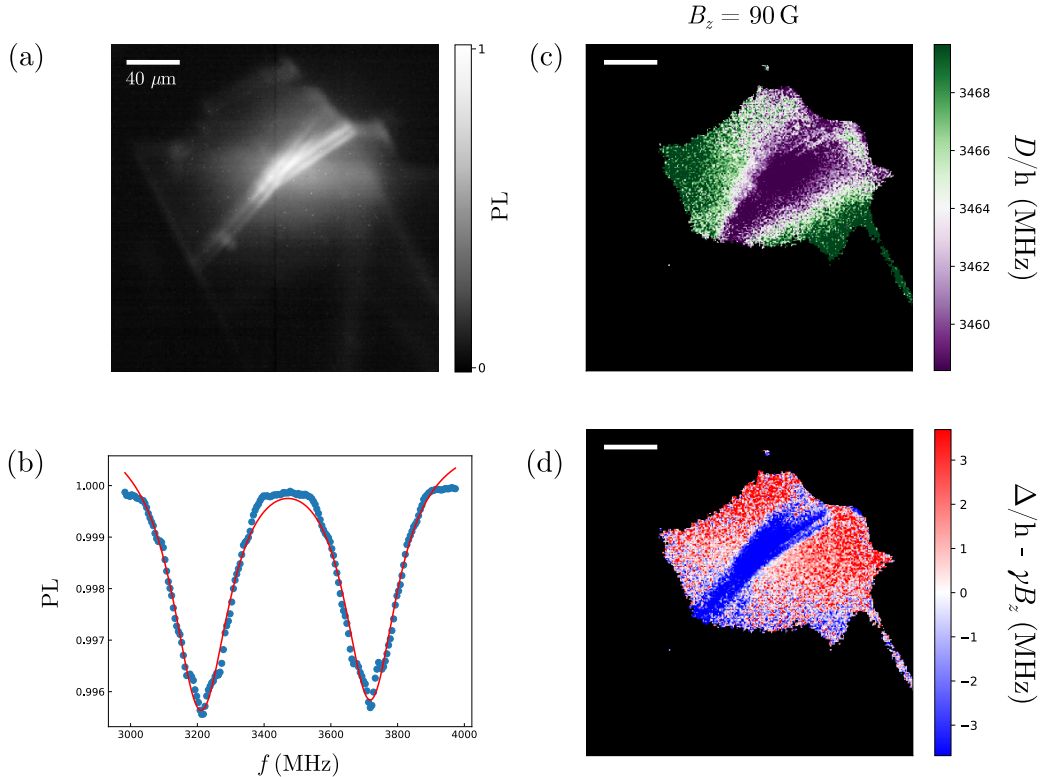


Figure 3.5: Widefield ODMR of a relatively uniform hBN flake. (a) PL image. (b) ODMR response averaged over the entire image. Blue points are measured data, red line is a fit of the sum of two Lorentzians. (c) D -map. (d) Strain and magnetic field map.

3.5 Outlook

As we have seen, the V_B^- in hBN can certainly be used for widefield ODMR at room temperature, with little a modification to existing setups designed for NV. This opens up a vast field of enquiry, particularly in the realm of strain interactions. That the spin defect is similar to the NV⁻ immediately raises the prospect of employing techniques such as NMR and hyper-polarization to hBN. Being a van der Waals (vdW) material, hBN with embedded V_B^- or other quantum defects has the exciting potential of being used in a complementary manner with other vdW materials, where it is already routinely employed to form a heterostructure for passivation or insulation [22].

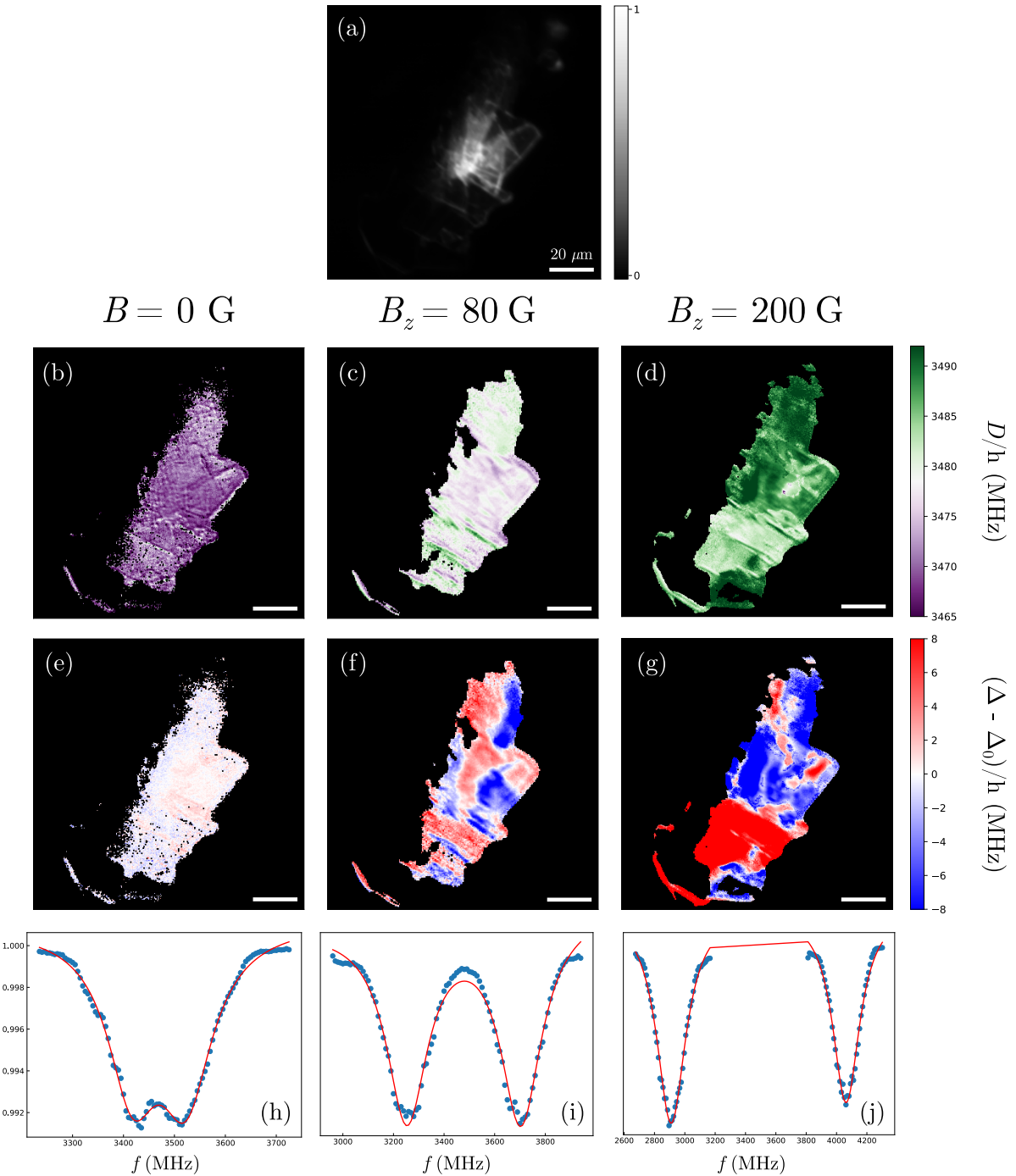


Figure 3.6: Widefield ODMR of a complex hBN flake. (a) PL image. (b-j) Each column is from a single data-set, with bias magnetic field increasing from left (0 T) to right (~ 200 G). (b-d) D -maps. Black region indicates where the Lorentzian fits failed, which correlates to low PL in (a) i.e. regions where there is either no hBN or limited laser illumination. (e-f) Strain and magnetic field maps. The mean component Δ_0 has been subtracted from each image. In (e), $B_z = 0$ G hence $\Delta_0 = E$. In (f) and (g), $B_z \gg E$ hence $\Delta_0 = B_z$. (h-j) ODMR response averaged over the entire image. Blue points are measured data, red lines are a fit to the sum of two Lorentzians.

Chapter 4

Application of Widefield Quantum Microscopy to Imaging Photocurrents in Photovoltaic Devices

Improving solar cell power conversion efficiency (PCE) is a vital ongoing challenge [87, 88]. For progress to continue, advanced techniques for electro-optical characterisation are required at all scales, from angstroms to meters, and at all stages of production, from cell design research to manufacturer processing quality [89]. Existing techniques to spatially map current flow at the single cell scale include lock-in thermography, whereby electrical heating is used to identify current flow and local sites of inefficiency [90]. Other techniques are laser or electron beam induced current mapping [91–93], described in Section 4.3. Compared with these methods, widefield NV[−] imaging can directly sense charge current flow, by imaging the induced magnetic field, thus providing a novel view into the operation of a solar cell.

In 2020, our group began a project to study the applicability of widefield NV[−] microscopy to charge transport imaging in photovoltaic (PV) devices. Research grade and commercial solar cells were provided by collaborators at the Australian National University and at the University of Melbourne. In-house PV devices were fabricated by Brett Johnson. Sam Scholten constructed a multi-beam widefield NV[−] microscope designed specifically for PV imaging. While the main focus of this project is to demonstrate sensing of photocurrents in PV devices using NV[−] magnetometry, here I will focus on my specific contributions. These included building and operating a laser beam induced current (LBIC) mapping device for cell characterisation, COMSOL modelling to guide and inform the NV[−] imaging experiments, and attempts to improve magnetic field alignment to reduce the impact of the bias magnetic field on the images. The work presented in Chapter 2 was also motivated by the need to improve image resolution and reduce artefacts in measurements of charge current in solar cells.

4.1 Principles of Current Mapping with NV

The capability of widefield NV[−] magnetometry to perform imaging of charged current flow has been reported using a variety of electronic devices [32, 33, 35, 94], including photocurrents [95], and biological samples [96]. This is possible by inversion of the Biot-Savart law, which describes the Øersted field $\mathbf{B}(\mathbf{r})$ due to a current distribution \mathbf{J} ,

$$\mathbf{B}(\mathbf{r}) = \frac{\mu_0}{4\pi} \int d^3\mathbf{r}' \frac{\mathbf{J}(\mathbf{r}') \times (\mathbf{r} - \mathbf{r}')}{|\mathbf{r} - \mathbf{r}'|^3}, \quad (4.1)$$

where μ_0 is the vacuum permeability and the integral is over all space. There are a number of methods to calculate the in-plane current density \mathbf{J} from \mathbf{B} . Here we use the in-plane components B_x and B_y (simultaneously measured with NV vector magnetometry), which has been demonstrated to induce the least artefacts in the reconstruction of current densities[70]. Assuming the thin-film limit (\mathbf{J} confined to the xy plane and $J_z(\mathbf{r}) = 0$), Eq. 4.1 can be inverted in Fourier space to reconstruct the current flow from the imaged stray magnetic field,

$$(B_x, B_y) \rightarrow \begin{cases} \mathcal{J}_x = -\alpha \mathcal{B}_y \\ \mathcal{J}_y = +\alpha \mathcal{B}_x \end{cases}, \quad (4.2)$$

where $\mathcal{J}(k_x, k_y)$ is the Fourier-space current density, $\mathcal{B}(k_x, k_y)$ is the Fourier-space magnetic field in the NV[−] plane, (k_x, k_y) is the 2D wave vector (transformed position vector) with $k = \sqrt{k_x^2 + k_y^2}$ and

$\alpha = 2e^{k\Delta z/\mu_0}$ for an average NV-sample standoff of Δz . A fundamental limitation to this technique is that arbitrary currents in 3-dimension cannot be reconstructed from the stray field alone¹ - thus additional geometric constraints must be imposed. As such this technique is best suited to imaging current flow in 2D planar devices, for which current flow may be reconstructed under the constraint that it is entirely in the plane of the device.

4.2 Theory of Photovoltaic Cells

Photovoltaic cells operate on the principle of charge separation, which can be induced in a number of ways [97]. Traditionally, a bulk material (such as silicon) is treated with two dopants, forming an N-type (electron majority carrier) region and a P-type (hole majority carrier) region. This is known as a PN junction [Fig. 4.1 (a)]. At the boundary of the regions, there is a depletion layer where electrons and holes recombine. Incident photons generate electron-hole pairs, resulting in a charge imbalance. With a connected external load, the resulting drift-diffusion forces will cause charge flow through the external circuit, doing useful work. It is also possible for charge separation to occur without the inbuilt electric field provided by a PN junction, for example in the case of heterocontact designs, in which the bulk is low-dopant, and the contacts are electron/hole selective [98]. A major improvement to PV efficiency came with the development of interdigitated back contacts (IBCs), in which the metal contacts are entirely on the back side of the cell, eliminating the loss due to optical shadowing [Fig. 4.1 (b)].

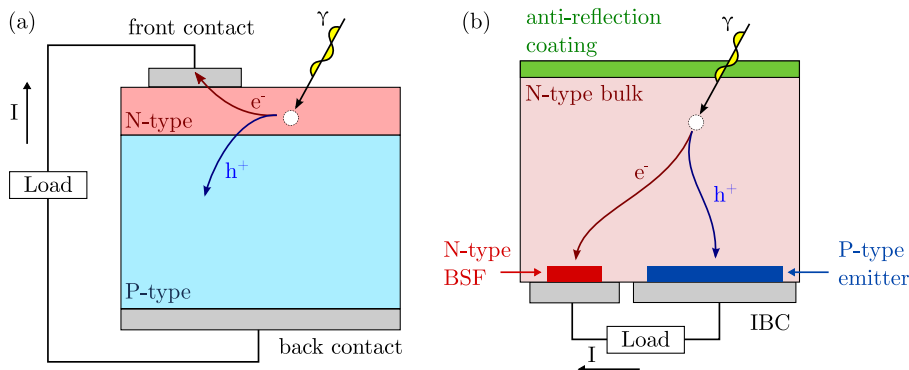


Figure 4.1: (a) Standard PN cell. (b) Interdigitated back contact (IBC) cell with back surface field (BSF) N-type and P-type emitter collectors - these are highly doped regions resulting in effectively selective contacts.

4.3 Implementation of a Light Beam Induced Current Mapping Device

Starting in the 1980s, laser beam induced current (LBIC) mapping has been utilised as an effective tool for non-destructive characterisation of photo-electric devices [92, 99, 100]. Although LBIC can be used to measure a number of quantitative electrical properties, such as internal (external) quantum efficiency - the ratio of total (absorbed) incident photons to electrons collected - here it was used to qualitatively establish whether devices - both fabricated in-house and commercial cells - were functioning as expected.

4.3.1 Setup

The experimental setup is shown in Fig 4.2. Excitation source is a solid-state laser emitting at $\lambda = 532$ nm (Laser Quantum Gem 532) focused by an objective (Olympus UPlanSApo 100x, NA = 1.4). The PV device is mounted to an XYZ stage, for lateral (XY) scanning and focusing (Z). In order to take high resolution scans over a large area, the XYZ stage was composed of two robotic stages: a course stepped

¹Widefield NV⁻ sensing typically images the stray field in a plane, however this is a general result even when the full stray field is known.

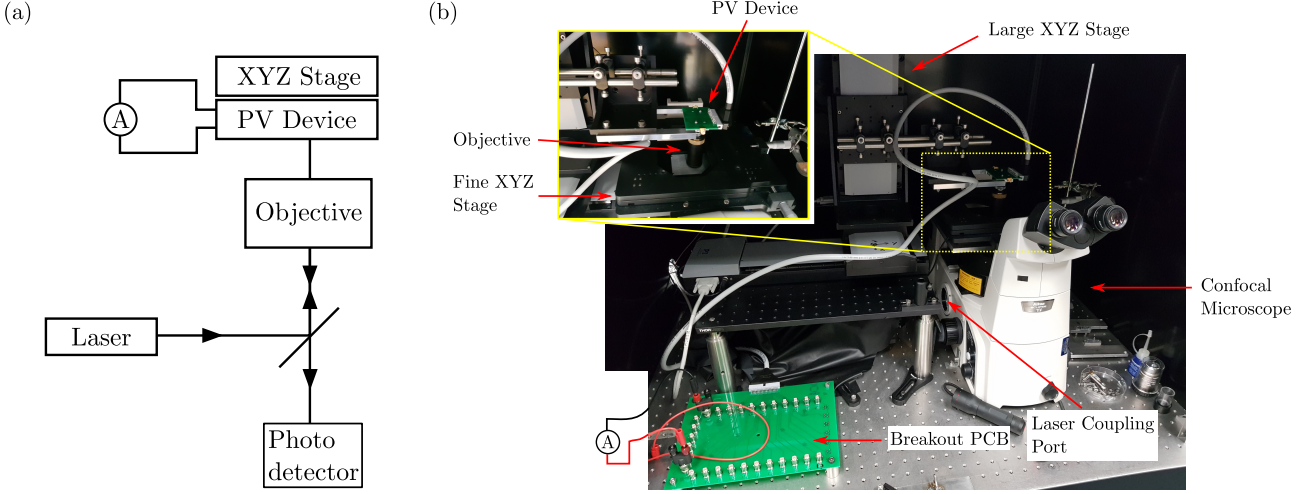


Figure 4.2: (a) Schematic of the light beam induced current (LBIC) mapping experiment. The photodetector is used to simultaneously map the device reflectance, which aids in spatially correlating the LBIC map. (b) Photograph of the LBIC setup, showing the confocal microscope, scanning stages and photovoltaic device. Ammeter is indicated diagrammatically. Not shown is the beam path, which is coupled in from under the breadboard to which the large stage is mounted.

XYZ stage (Newport), and a fine stepped XY stage (PI P-611.3 NanoCube). Fixed voltage current measurements were performed using a Kiethly source measure unit (SMU). The epifluorescence beam is directed to a photodetector for optical imaging, and also used to bring the PV device into focus.

Using LabView, I wrote a program to utilise both stages to stitch together high resolution scans. The program takes as input the number of ‘chunks’ to scan (e.g. 5×5), the size of each chunk (e.g. $200 \mu\text{m} \times 200 \mu\text{m}$) and the step-size (e.g. $1 \mu\text{m}$). The Kiethly voltage is set (typically 0 V) and the laser power is set (e.g. 50 mW). The program then scans across the specified area, at each pixel recording an electric current value and optical signal.

4.3.2 Results

The LBIC system was first applied to in-house fabricated PV metal-semiconductor-metal (MSM) device [Fig. 4.3 (b)], composed of an intrinsic crystalline silicon bulk absorber, aluminium contacts, and As doping between the contacts. The device was imaged using LBIC scanning under zero, positive and negative bias conditions. In each scan, two terminals (one on the left and one on the right) were connected through the SMU which provided voltage control and current measurements. The resulting maps in Fig. 4.3 (d-f) respectively demonstrate the device is photo-active, as there is significantly increased current flow when the laser spot is over the doped silicon compared with the contact metal. As seen in Fig. 4.3 (c), the contact edge is also a junction edge (between N-type Si and intrinsic Si), hence the observed current decay away from the edge is expected to be exponential and related to the minority carrier diffusion length [101]. The asymmetry in Fig. 4.3 (e-f) can be understood by considering the introduction of a bias current to the symmetric case in Fig. 4.3 (d): a positive bias will increase the positive current flow and suppress negative current flow, and vice-versa.

4.4 Computational Modelling

To develop an intuition for the currents we would be imaging, particularly of a heterocontact design, I undertook a small qualitative modelling project. In particular, we needed a simulation tool which output the internal cell current flow, to inform the NV^- current imaging experiment. Although all solar cell simulators must calculate the current internal flow, in general standard simulation outputs are only the terminal measurements (net current, voltage), which relate better to existing measurement techniques.

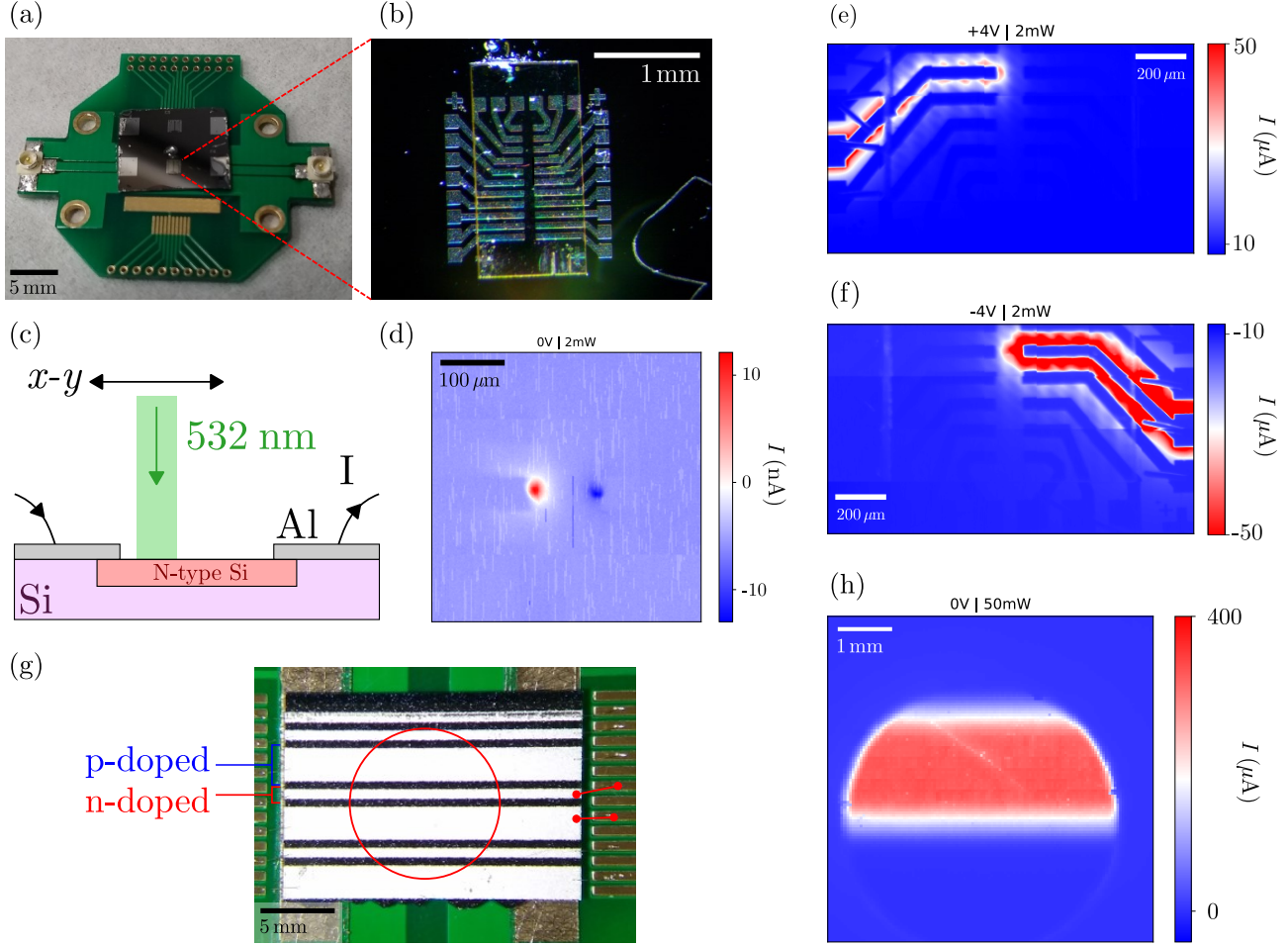


Figure 4.3: (a) The metal-semiconductor-metal (MSM) device mounted to a breakout printed circuit board (PCB). (b) Closeup of the device. The NV-embedded diamond on top is not used for light beam induced current (LBIC) mapping, but is used for NV⁻ current mapping. (c) Illustration depicting the in-house photovoltaic device. A 532 nm beam was used for LBIC mapping (in practice, the sample was scanned and the beam held static). (d-f) LBIC maps of the device, with zero, positive and negative bias applied respectively. Header indicates applied bias voltage and laser power. (g) Back face of a cut-down commercial (SunPower) solar cell mounted to the PCB. The opposite side of the PCB has a hole cutout (red circle) to shine the beam through. (h) LBIC map of the solar cell, mapping the circled area in (g). Comparing (h) with the MSM device (d), we see the SunPower cell has a larger diffusion length. Headers indicate applied bias voltage and laser power.

Initially I used a 2D model, however it became apparent that the dynamics we initially sought to understand could be considered in 1D, significantly reducing the model complexity and simulation time. The 1D simulations allowed us to explore two important situations: current flow from electron selective contact to hole selective contact, and closed current loops involving a single electron/hole selective contact. The path of these closed loops can be modelled in 1D by identifying the boundaries.

Modelling was performed using the COMSOL Semiconductor module, largely due to its accessibility. For more detailed simulations, PV specific tools such as Quokka [102] would be more suitable. Light excitation was modelled as Gaussian curve of electron/hole pair generation. The bulk material is intrinsic Si, with ‘selective’ contacts modelled by heavily doping at the edges of the model, with the boundary points modelled as metal contacts. The key finding was the role that symmetry played: for internal current generation to occur, either the contacts had to be asymmetric (one electron selective, the other hole selective) or the laser excitation had to be off centre. Similar results are reported in [101]. The situation in which an off centred laser beam generates current with symmetric contacts corresponds to closed current loops in an open circuit device, or current flow in a closed circuit device. The latter explains the

initially unexpected observation of current flow in that device, seen in Fig. 4.3 (d).

4.5 Spatio-temporal Electric Current Imaging with NV

4.5.1 Setup

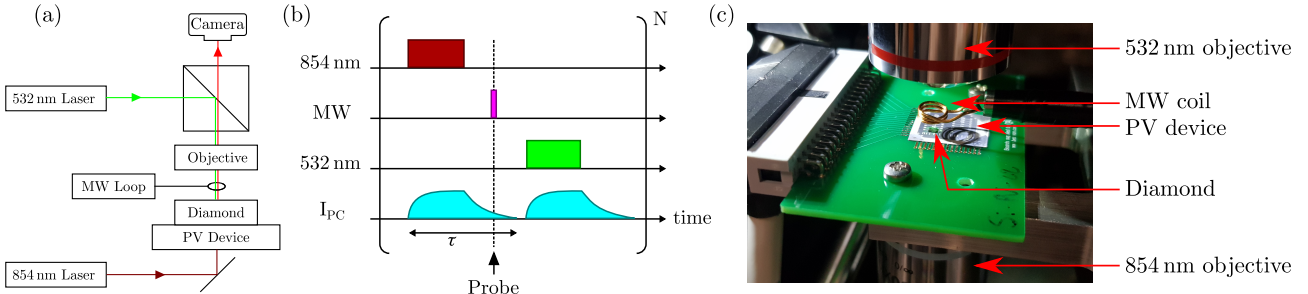


Figure 4.4: (a) Schematic of the widefield NV⁻ microscope for current imaging. (b) Dynamical pulse sequence as described in the text. (c) Photograph of the photovoltaic device in the widefield microscope.

The construction and operation of a widefield quantum diamond microscope purpose built for PV current imaging was carried out by Sam Scholten from 2020-21 [103]. Briefly, the system consists of two anti-parallel laser beams impinging the cell. The first is the 532 nm NV⁻ excitation beam, and the second is a near infrared (NIR) 854 nm beam used for electron-hole pair generation. The NIR beam excites the sun-facing side of the cell, while the excitation beam addresses NVs embedded in a diamond probe on the back face of the cell [Fig. 4.4(a)]. A dynamical pulse sequence [Fig. 4.4 (b)] was designed to temporally probe the photocurrent, by varying the NV⁻ probe time with respect to the NIR photoexcitation pulse. First, the NV⁻ ensemble is initialised (spin-0 polarised) as usual with 532 nm excitation. Next, the NIR pulse generates photocurrents in the solar cell. Either during or after the NIR pulse, at a time delay τ , a microwave π -pulse drives the NV⁻ $|0\rangle_g \rightarrow |\pm 1\rangle_g$ transition, thus capturing a snapshot of the photocurrent induced magnetic field. Following the π -pulse, readout is performed using another 532 nm pulse, which also acts as initialisation for the next iteration. This sequence is repeated N times and integrated to achieve a sufficient signal to noise ratio. By sweeping τ , a full dynamical picture of the photocurrent can be attained, capturing the rise, steady state, and subsequent decay.

4.5.2 Preliminary results

Using the dynamic pulse sequence, various devices were imaged including an in-house fabricated heterocontact cell. The cell consists of an intrinsic crystalline silicon bulk absorber, on which MoO_x (hole selective), LiF (electron selective) and aluminium (contacting) layers are evaporated, as seen in Fig. 4.5 (c). In the experiment shown in Fig. 4.5 (e-h), NIR illumination excites a spot near a hole selective contact, which is otherwise not connected to any external circuit. This corresponds to the COMSOL situation in Fig. 4.5 (a) under the 1D↔2D correspondence described above and shown in Fig. 4.5 (c). As expected, current loops occur, with the charges following return paths in preference of least resistance [101]. This successfully demonstrates the capability of widefield quantum imaging to measure photocurrents in PV devices. The quantitative vector field attained can be used for further analysis, such as integrating the total current flow across sections of the cell.

4.5.3 Engineering the Bias Field

In addition to the interfacing problem discussed in Chapter 2, the bias magnetic field required in wide-field imaging introduces a background field gradient. This causes two problems.

Firstly, there is a non-linear gradient superimposed on the imaged stray field, which must be removed to recover the stray field due to the device (here generated by photocurrents) only. This can be achieved by taking a reference image with no device present, and subtracting it from subsequent images. However, taking a reference image is not always practical, and when it is, combining the images results in a $2\times$

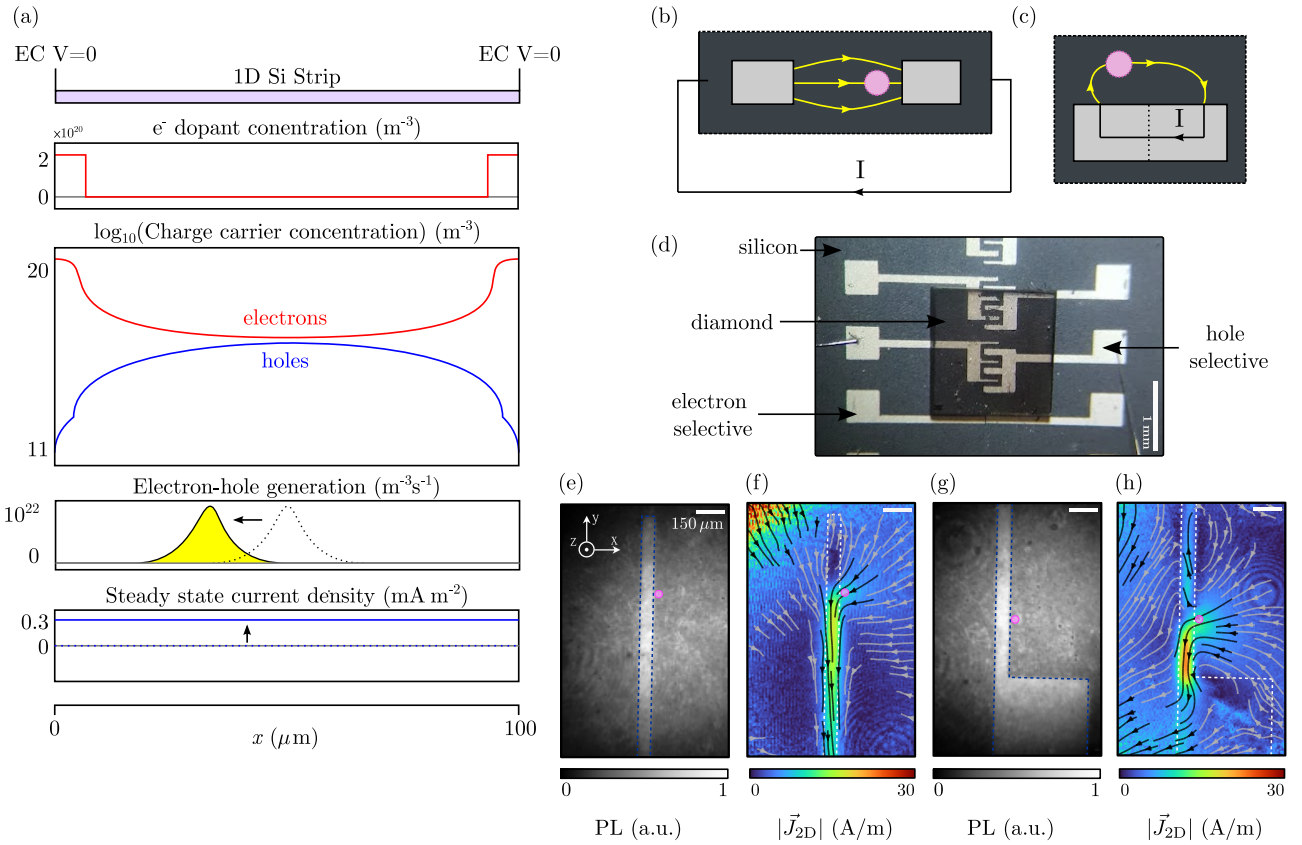


Figure 4.5: (a) COMSOL simulation setup and results, for the 1D symmetric N-doped case corresponding to 2D current loops through a hole-selective contact. When the electron-hole pair generation is centred (dashed line), no steady state current is measured (dashed blue line). When the generation is offset (solid line, yellow fill), a current is observed (solid blue line). (b) Schematic of the 2D closed circuit situation corresponding to the 1D simulation. Pink spot indicates near-infrared (NIR) illumination. Yellow lines indicate electron-hole current flow. (c) Schematic of the 2D open circuit situation corresponding to the 1D simulation. Dashed line in the contact marks the effective ‘external circuit’. (d-h) Images of a hole-selective contact on an N-doped silicon substrate. None of the contacts on this device are connected to any external circuit. (d) Fluorescence image of the device. (e) Fluorescence image, with pink spot indicating NIR illumination. (f) Current map reconstructed from NV⁻ measurements of the induced \mathbf{B} field. Black (grey) stream vectors indicate high (low) current density. (g) Fluorescence image similar to (c), with a different illumination point. (h) Comparing with (d), we see the current paths differ, due to the different resistance of the possible return paths. Panels (b-f) reproduced from [103].

increase in the random noise present in the result. Alternatively, a background field gradient can be fitted to the image, or to the reference to remove the introduction of noise. However, fitting a non-linear background is a challenge, particularly in the absence of a reference image where it is important to not remove the signal along with the background. In some cases, such as in Chapter 2, subtracting a first order correction is sufficient. The correction is produced by fitting a linear gradient to the points thought to be without signal caused by the sample. In contrast, for current imaging the device stray field is not well characterised, so even selecting points for fitting is a difficult prospect.

Secondly, the variation in field permeating the NV⁻ defect ensemble volume results in an increased dephasing rate, or reduced T_2^* [104] (as described in 1.1.4). In particular, for pulsed sequences the inhomogeneity limits NV⁻ contrast and sensitivity [12]. This effect cannot be resolved with post-processing, it requires engineering of a homogeneous magnetic field.

There are a number of methods to address the bias-field engineering. The simplest method to create a bias field is to use a single, strong permanent magnet. Improving on this, one can use a second permanent magnet, resulting in a more uniform zone between the magnets. Rather than permanent magnets,

electromagnets in a Helmholtz coil configuration can also create a uniform zone, introducing benefits such as easier control over the field strength at the sample, and complexities such as power supply and sample heating [12]. Introducing additional correction (“shim”) coils, it is possible to achieve bias fields with uniformity better than 1 part-per-billion over a centimetre-scale volume [105].

For this project, simplicity and space-constraints were the priority. Structurally, the dual-beam optical system requires optics above and below the sample, in addition to the microwave driver adjacent to the sample, leaving little room for electromagnetic coils. For their simplicity and compactness, permanent magnets were chosen, and I undertook a small project to optimise them as best as possible.

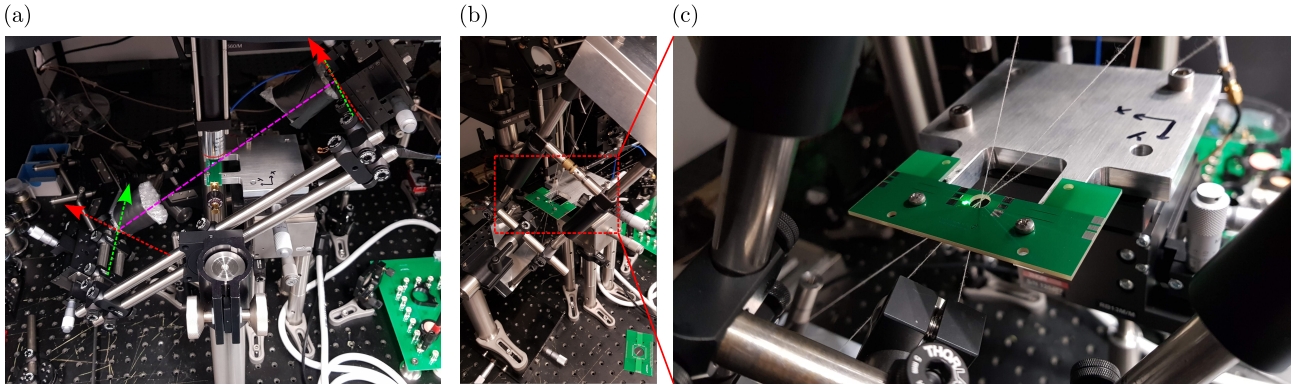


Figure 4.6: (a) Configuration 1: Two smaller magnets, each mounted to lateral 2D stages. Dashed purple line indicates magnet axis, green and red arrows indicate lateral translation of magnets. (b) Configuration 2: Two larger magnets, fixed in relative alignment. (c) String alignment of configuration 2. The printed circuit board (PCB) with the hole at the centre is removed after alignment and replaced with a PCB hosting the sample, positioned in the same location as the hole.

The first configuration explored was lateral adjustment of two magnets, as seen in Fig. 4.6 (a). To simulate the field produced, I adapted a code which models the magnetic field produced by magnetic ‘bits’, where each bit is a parallelepiped producing a uniform magnetisation [54]. The total vector field due to each bit is calculated in the sensing plane, then projected onto the NV-axis to determine the final magnetic image. Here, the bias magnets are modelled using a single bit each, with the sensing plane between them. I simulated an optimisation procedure whereby the maximum magnetic variation over the image $V = \max(|\mathbf{B}|) - \min(|\mathbf{B}|)$ is minimised in two steps. In step one, a single magnet is added, and is moved laterally. As expected, plotting V against lateral offset showed that minimum V was achieved at zero offset. In step two, a second magnet is added at an equal and opposite distance from the sample. Again the simulation confirmed that V increased monotonically with lateral offset, indicating this could be used for alignment.

To determine $|\mathbf{B}|$ experimentally, the bias field angle was chosen such that all four NV^- families were visible in the ODMR spectrum, yielding the full over-constrained vector information. Selecting the three most split families (those most aligned with the bias field, hence least influenced by strain), solving for \mathbf{B} simply requires inversion of

$$\begin{pmatrix} u_x^1 & u_y^1 & u_z^1 \\ u_x^2 & u_y^2 & u_z^2 \\ u_x^3 & u_y^3 & u_z^3 \end{pmatrix} \begin{pmatrix} B_x \\ B_y \\ B_z \end{pmatrix} = \begin{pmatrix} B_1^{\text{meas}} \\ B_2^{\text{meas}} \\ B_3^{\text{meas}} \end{pmatrix}, \quad (4.3)$$

where \mathbf{u}^i is the unit vector along the i^{th} NV^- family axis, \mathbf{B} is the bias field, and \mathbf{B}^{meas} are the measured components of the bias field projected along the NV^- axes. Note that another method to recover \mathbf{B} is to numerically solve the over-constrained problem where the projections from all four NV^- families are used. Experimentally, measuring the uniformity of $|\mathbf{B}|$ using V is error prone, due to single pixel errors

and random noise. Instead, for each magnetic image I took a histogram of $|B|$, and used the FWHM to compare the uniformity measured in different situations.

In practice, I found that although this optimisation method can be used to align the magnets, it does not result in a better field uniformity than can be achieved simply by aligning the magnets by eye. To test a different alignment method, I used string to determine the midpoint between the two large magnets, as seen in Fig. 4.6 (c). Again this did not result in improved uniformity. There are a number of explanations for why the uniformity could not be improved by better alignment. Firstly, there is the possibility that the magnetisation vectors of the magnets do not align with their form, meaning that the magnetic axis are not aligned. Addressing this is challenging, as it requires careful characterisation of the permanent magnet, beyond the scope of this project. Secondly, the random background field due to magnetised objects on the lab bench could limit the attainable field uniformity, without the introduction of shim coils.

In addition to varying simulating lateral offsets, I also simulated magnets of different sizes. The simulation result was encouraging: doubling the size of the magnet led to an order of magnitude improvement of the magnetic field gradient, when the larger magnets were placed further away to attain the same field strength at the sample as with the smaller magnets. Guided by this result, and the previous result that in practice fine alignment led to negligible improvement, I constructed a second bias-magnet rig using much larger magnets. I also removed as much equipment from the bench as possible, including distancing the para-magnetic translation stage from the sample by introducing a long arm to hold the sample. Unfortunately, whether these changes caused any systematic improvement to field homogeneity was inconclusive. The bias gradients measured experimentally were very similar to the case with two small magnets, after alignment. There did appear to be a slight benefit to using the large magnets, which is that the homogeneity was not as sensitive to their position compared with small magnets. Thus the outcome of this effort was that large magnets are slightly preferable in practice, but more sophisticated techniques are required if bias field homogeneity is to be significantly improved.

4.6 Outlook

Research into solar cell design is advancing at a rapid pace. While silicon based cells are at present the industry standard [89], other materials such as hybrid organic-inorganic perovskite materials are emerging with efficiencies competitive to silicon cells [106, 107]. Perovskite based cells require advanced architectures to overcome a number of fabrication and operational problems. In collaboration with Dr. Anthony Chesman (CSIRO), we intend to apply the novel photocurrent imaging solution described in this chapter to perovskite cells with novel honeycomb back-contact electrodes, where the ability to resolve the spatial distribution of current flow with high current sensitivity may provide useful information given the collection efficiencies have found to be highly geometry dependent [107].

Some future improvements to the widefield NV photocurrent imaging system are as follows. An increased field of view, covering multiple diffusion lengths, would give a more complete picture of the internal current distributions. Additionally, a wider field of view would allow pixel binning (averaging), increasing the sensitivity and reducing measurement time (at the cost of spatial resolution). Thus far, our photocurrent measurements have required a long dark-time between the NIR and green pulse, to ensure the photocurrent measured is due to the NIR pulse only. With the addition of a laser shield (~ 100 nm) between the diamond and PV device, the green laser would not illuminate the PV device hence this dark-time could be reduced, reducing signal interference and further speeding up the measurement time. Finally, improving reconstruction methods, including developing 3D models to facilitate super-resolution techniques, would enable imaging currents not confined to a 2D plane.

A report of the photocurrent measurements discussed here, and additional measurements of a similar nature, is currently being prepared for publication [103].

Concluding remarks and future work

This thesis presented the novel design, implementation and testing of a widefield quantum microscope, and experimental work in state-of-the-art materials and industrial applications. Chapter 1 introduced the concept of the quantum widefield microscope, providing a background to spin-defect based quantum sensing with a focus on the current ‘sensor of choice’ - the nitrogen-vacancy (NV) in diamond. The theory developed, together with empirical results, provided a framework for understanding the physical basis for and operational parameters involved in widefield quantum microscopy.

Chapter 2 addressed a longstanding issue of practicality for widefield NV microscopy: minimising the standoff between the sample and diamond without requiring either direct fabrication of the sample onto the diamond, or a burdensome trial and error approach. I designed a widefield probe, constructed a compact widefield NV quantum microscope, and performed a rigorous analysis of its performance, namely image resolution and best achieved standoff. Using an interference based alignment technique, I showed that it is possible to systematically perform high resolution imaging. Further work includes performing optical characterisation of the system (imaging a high resolution target), as well as implementing a number of features such as automation of alignment, designed to increase the throughput of the device without sacrificing performance or reliability.

Chapter 3 presented a preliminary study of widefield quantum microscopy with the boron vacancy (V_B^-) defect in hexagonal boron nitride (hBN). It outlined the recent emergence of the V_B^- in hBN as a quantum sensor and the exciting advantages it might offer over the NV in diamond. These include its thin layer van der Waals structure, and ability to conform to the sample under investigation, meaning it may provide an alternative solution to the standoff challenge addressed in Chapter 2. Experimental results were communicated, including world-first ODMR widefield images I took of hBN flakes, revealing a complex interplay between its strain, temperature and magnetic properties. I also performed some initial measurements of the spin dynamics. Quantum sensing with the V_B^- is largely uncharted territory - the state of knowledge is currently approximately equivalent to that of the NV over a decade ago. There is therefore enormous scope for future study, characterisation and optimisation of the sensor. The focus for our group going forward will be widefield sensing with hBN, including spin-dynamics, dynamical temperature sensing, and demonstrations of application to 2D material physics.

Chapter 4 illustrated how widefield quantum microscopy can be applied to real world challenges, through the development and application of a novel domain specific quantum microscope to image the internal photocurrents of solar cells. My contributions to this project have been simulation and modelling, and constructing a light beam induced current mapping device, presently one of a number of industry standard photo-voltaic characterisation tools. With the capability of widefield quantum sensing for photocurrent imaging firmly established [103], future directions include imaging the photocurrent dynamics of emerging technologies such as perovskite cells, and providing unique information on cell performance and deficiencies.

This foray into experimental condensed matter research, working at the cutting-edge of instrumentation and solid-state spin-defect physics, has been an exhilarating and enlightening journey. Our goals for the next months and year are perhaps even more exciting, including unprecedented investigations into the physics of a newly discovered quantum material (hBN), potentially capable of providing insights into some of the most fascinating physical phenomena (physics in 2D materials such as graphene) being explored today. Other projects are the development of a next generation microscope incorporating advanced technology to deliver a more practical platform for widefield imaging, and bringing widefield microscopy to use in the development of next generation solar cells. Experimental and theoretical physics, and engineering, are all at play, hopefully eventuating in breakthrough understandings in physics, and the development of positive technologies to address the challenges we face as a rapidly developing civilisation.

References

- [1] V. M. Acosta et al., *Journal of Superconductivity and Novel Magnetism* **32**, 85 (2019) (cit. on p. 2).
- [2] D. A. Simpson, *Nano Today* **24**, 7 (2019) (cit. on p. 2).
- [3] F. Casola et al., *Nature Reviews Materials* **3**, 17088 (2018) (cit. on p. 2).
- [4] S. E. Crawford et al., *Advanced Quantum Technologies* **4**, 2100049 (2021) (cit. on p. 2).
- [5] S. C. Scholten et al., *Journal of Applied Physics* **130**, 150902 (2021) (cit. on pp. 2, 3, 6, 8–10, 24).
- [6] Y. Schlussel et al., *Phys. Rev. Appl.* **10**, 034032 (2018) (cit. on p. 2).
- [7] S. E. Lillie et al., *Nano Lett.* **20**, 1855 (2020) (cit. on p. 2).
- [8] D. M. Toyli et al., *Phys. Rev. X* **2**, 031001 (2012) (cit. on p. 2).
- [9] M. Lesik et al., *Science* **366**, 1359 (2019) (cit. on p. 2).
- [10] S. Hsieh et al., *Science* **366**, 1349 (2019) (cit. on p. 2).
- [11] L. Toraille et al., *New J. Phys.* **22**, 103063 (2020) (cit. on p. 2).
- [12] E. V. Levine et al., *Nanophotonics* **8**, 1945 (2019) (cit. on pp. 2, 3, 41, 42).
- [13] R. R. Fu et al., *Geochem. Geophys. Geosystems* **21**, e2020GC009147 (2020) (cit. on pp. 2, 3, 20, 22).
- [14] J. R. Maze et al., *Nature* **455**, 644 (2008) (cit. on pp. 2, 3).
- [15] J. M. Taylor et al., *Nature Physics* **4**, 810 (2008) (cit. on pp. 2, 3).
- [16] L. Rondin et al., *Rep. Prog. Phys.* **77**, 056503 (2014) (cit. on pp. 2, 3, 5, 15, 16).
- [17] F. Casola et al., *Nat. Rev. Mater.* **3**, 17088 (2018) (cit. on pp. 2, 3, 18, 19).
- [18] D. Simin, “Quantum Sensing with Highly Coherent Spin Centers in Silicon Carbide” (Universität Würzburg, 2017) (cit. on p. 2).
- [19] S. Castelletto et al., *2*, 022001 (2020) (cit. on p. 2).
- [20] A. Gottscholl et al., *Nature Materials* **19**, 540 (2020) (cit. on pp. 2, 27, 28, 30, 32).
- [21] F. F. Murzakhanov et al., *Nanomaterials* **11**, 1373 (2021) (cit. on p. 2).
- [22] J.-P. Tetienne, *Nature Physics*, 1 (2021) (cit. on pp. 2, 34).
- [23] K. S. Burch et al., *Nature* **563**, 47 (2018) (cit. on p. 2).
- [24] A. Gottscholl et al., *Nature Communications* **12**, 4480 (2021) (cit. on pp. 3, 32, 33).
- [25] G. Davies et al., *Proceedings of the Royal Society of London. A. Mathematical and Physical Sciences* **348**, 285 (1976) (cit. on p. 3).
- [26] S. Steinert et al., *Rev. Sci. Instrum.* **81**, 043705 (2010) (cit. on pp. 3, 8).
- [27] J. M. McCoey et al., *Small* **15**, 1805159 (2019) (cit. on p. 3).
- [28] L. Toraille et al., *Nano Lett.* **18**, 7635 (2018) (cit. on pp. 3, 22).
- [29] D. A. Broadway et al., *Adv. Mater.* **32**, 2003314 (2020) (cit. on pp. 3, 19).
- [30] I. Meirzada et al., *ACS Nano* **15**, 5574 (2021) (cit. on p. 3).
- [31] G. Nava Antonio et al., *J. Appl. Phys.* **129**, 223904 (2021) (cit. on p. 3).
- [32] A. Nowodzinski et al., *Microelectronics Reliability* **55**, 1549 (2015) (cit. on pp. 3, 36).
- [33] J.-P. Tetienne et al., *Sci. Adv.* **3**, e1602429 (2017) (cit. on pp. 3, 36).
- [34] M. J. Turner et al., *Phys. Rev. Applied* **14**, 014097 (2020) (cit. on pp. 3, 22).
- [35] M. J. H. Ku et al., *Nature* **583**, 537 (2020) (cit. on pp. 3, 36).
- [36] D. Le Sage et al., *Nature* **496**, 486 (2013) (cit. on pp. 3, 25).
- [37] D. R. Glenn et al., *Nat. Methods* **12**, 736 (2015) (cit. on p. 3).
- [38] I. Fescenko et al., *Phys. Rev. Applied* **11**, 034029 (2019) (cit. on p. 3).
- [39] J. M. McCoey et al., *Small Methods* **4**, 1900754 (2020) (cit. on p. 3).
- [40] R. R. Fu et al., *Science* **346**, 1089 (2014) (cit. on p. 3).
- [41] D. R. Glenn et al., *Geochem. Geophys. Geosystems* **18**, 3254 (2017) (cit. on pp. 3, 25).
- [42] M. W. Doherty et al., *New Journal of Physics* **13**, 025019 (2011) (cit. on pp. 3, 4).
- [43] S. Sharma et al., *Physical Review A* **101**, 043420 (2020) (cit. on p. 4).
- [44] S. Karaveli et al., *Proceedings of the National Academy of Sciences* **113**, 3938 (2016) (cit. on p. 4).
- [45] L. Robledo et al., *New Journal of Physics* **13**, 025013 (2011) (cit. on p. 5).

- [46] V. M. Acosta et al., *Physical Review B* **82**, 201202 (2010) (cit. on p. 5).
- [47] A. Jarmola et al., *Physical Review Letters* **108**, 197601 (2012) (cit. on p. 5).
- [48] A. Gottscholl et al., *Science Advances* **7**, eabf3630 (2021) (cit. on pp. 5, 32).
- [49] A. Dréau et al., *Physical Review B* **84**, 195204 (2011) (cit. on pp. 6, 7).
- [50] P. Jamonneau et al., *Physical Review B* **93**, 024305 (2016) (cit. on p. 7).
- [51] G. Balasubramanian et al., *Nature* **455**, 648 (2008) (cit. on p. 8).
- [52] J. R. Maze et al., *Nature* **455**, 644 (2008) (cit. on p. 8).
- [53] P. Maletinsky et al., *Nat. Nanotechnol.* **7**, 320 (2012) (cit. on p. 8).
- [54] L. Rondin et al., *Appl. Phys. Lett.* **100**, 153118 (2012) (cit. on pp. 8, 42).
- [55] J. P. Tetienne et al., *Science* **344**, 1366 (2014) (cit. on p. 8).
- [56] L. M. Pham et al., *New J. Phys.* **13**, 045021 (2011) (cit. on p. 8).
- [57] M. Chipaux et al., *Eur. Phys. J. D* **69**, 166 (2015) (cit. on p. 8).
- [58] D. A. Simpson et al., *Sci. Rep.* **6**, 22797 (2016) (cit. on pp. 8, 22).
- [59] L. Thiel et al., *Nat. Nanotechnol.* **11**, 677 (2016) (cit. on p. 8).
- [60] S. Ernst et al., *ACS Photonics* **6**, 327 (2019) (cit. on pp. 10, 17, 24).
- [61] G. J. Abrahams et al., *Submitted to Applied Physics Letters* (2021) (cit. on p. 10).
- [62] S. Dushenko et al., *Phys. Rev. Applied* **14**, 054036 (2020) (cit. on pp. 12, 24).
- [63] A. J. Healey et al., *Phys. Rev. Materials* **4**, 104605 (2020) (cit. on pp. 13, 24).
- [64] N. B. Manson et al., *New J. Phys.* **20**, 113037 (2018) (cit. on p. 13).
- [65] M. Capelli et al., *Carbon* **143**, 714 (2019) (cit. on p. 13).
- [66] I. Gross et al., *Phys. Rev. B* **94**, 064413 (2016) (cit. on pp. 15, 20).
- [67] M. W. Doherty et al., *Phys. Rep.* **528**, 1 (2013) (cit. on p. 15).
- [68] D. A. Broadway et al., *Nat. Electron.* **1**, 502 (2018) (cit. on p. 16).
- [69] E. A. Lima et al., *J. Geophys. Res. Solid Earth* **114**, B06102 (2009) (cit. on pp. 18, 19).
- [70] D. Broadway et al., *Phys. Rev. Applied* **14**, 024076 (2020) (cit. on pp. 18, 36).
- [71] T. Hingant et al., *Phys. Rev. Applied* **4**, 014003 (2015) (cit. on pp. 18, 19).
- [72] L. Thiel et al., *Science* **364**, 973 (2019) (cit. on p. 19).
- [73] J. Olivero et al., *Journal of Quantitative Spectroscopy and Radiative Transfer* **17**, 233 (1977) (cit. on p. 22).
- [74] I. Bertelli et al., *Sci. Adv.* **6**, eabd3556 (2020) (cit. on p. 22).
- [75] I. Meirzada et al., *ACS Nano* **15**, 5574 (2021) (cit. on p. 22).
- [76] J.-P. Tetienne et al., *Nature Communications* **6**, 6733 (2015) (cit. on p. 22).
- [77] A. Horsley et al., *Phys. Rev. Applied* **10**, 044039 (2018) (cit. on p. 25).
- [78] A. Przybylski et al., *Sci. Rep.* **7**, 15722 (2017) (cit. on p. 26).
- [79] J. D. Caldwell et al., *Nature Reviews Materials* **4**, 552 (2019) (cit. on p. 27).
- [80] T. T. Tran et al., *Nature Nanotechnology* **11**, 37 (2016) (cit. on p. 27).
- [81] J. R. Toledo et al., *Physical Review B* **98**, 155203 (2018) (cit. on p. 27).
- [82] A. L. Exarhos et al., *Nature Communications* **10**, 222 (2019) (cit. on p. 27).
- [83] J. R. Reimers et al., *Physical Review B* **102**, 144105 (2020) (cit. on p. 29).
- [84] J. E. Fröch et al., *Nano Letters* **21**, 6549 (2021) (cit. on p. 29).
- [85] D. A. Broadway et al., *Nano Lett.* **19**, 4543 (2019) (cit. on p. 34).
- [86] P. Udvarhelyi et al., *Phys. Rev. B* **98**, 075201 (2018) (cit. on p. 34).
- [87] A. Jäger-Waldau et al., *Pv status report 2019.* (2019) (cit. on p. 36).
- [88] D. B. Needleman et al., *Energy & Environmental Science* **9**, 2122 (2016) (cit. on p. 36).
- [89] G. M. Wilson et al., *Journal of Physics D: Applied Physics* **53**, 493001 (2020) (cit. on pp. 36, 43).
- [90] O. Breitenstein et al., *Quantitative InfraRed Thermography Journal* **16**, 203 (2019) (cit. on p. 36).
- [91] C. Donolato, *Journal of Applied Physics* **54**, 1314 (1983) (cit. on p. 36).
- [92] W. Qiu et al., *Science China Physics, Mechanics & Astronomy* **58**, 1 (2015) (cit. on pp. 36, 37).
- [93] P. R. Edwards et al., *Thin Solid Films*, 7 (2000) (cit. on p. 36).
- [94] A. Jenkins et al., (2020) (cit. on p. 36).

- [95] B. B. Zhou et al., *Phys. Rev. X* **10**, 011003 (2020) (cit. on p. 36).
- [96] L. T. Hall et al., *Scientific Reports* **2**, 401 (2012) (cit. on p. 36).
- [97] U. Würfel et al., *IEEE Journal of Photovoltaics* **5**, 461 (2015) (cit. on p. 37).
- [98] J. Bullock et al., *Nature Energy* **1**, 15031 (2016) (cit. on p. 37).
- [99] J. Bajaj et al., *Journal of Vacuum Science & Technology A* **5**, 3186 (1987) (cit. on p. 37).
- [100] B. Moralejo et al., *Journal of Electronic Materials* **39**, 663 (2010) (cit. on p. 37).
- [101] D. Redfern et al., *IEEE Transactions on Electron Devices* **53**, 23 (2006) (cit. on pp. 38–40).
- [102] A. Fell et al., *Solar Energy Materials and Solar Cells, Proceedings of the 7th International Conference on Crystalline Silicon Photovoltaics* **173**, 128 (2017) (cit. on p. 39).
- [103] S. C. Scholten et al., *Manuscript in preparation* (2021) (cit. on pp. 40, 41, 43, 44).
- [104] J. F. Barry et al., *Rev. Mod. Phys.* **92**, 015004 (2020) (cit. on p. 41).
- [105] L. M. K. Vandersypen et al., *Reviews of Modern Physics* **76**, 1037 (2005) (cit. on p. 42).
- [106] Q. Hou et al., *Nano Energy* **50**, 710 (2018) (cit. on p. 43).
- [107] X. Lin et al., *Nano Energy* **67**, 104223 (2020) (cit. on p. 43).